

The distribution of equivalent widths in long GRB afterglow spectra

A. de Ugarte Postigo^{1,2}, J.P.U. Fynbo², C.C. Thöne¹, L. Christensen², J. Gorosabel¹, B. Milvang-Jensen², S. Schulze³, P. Jakobsson³, K. Wiersema⁴, R. Sánchez-Ramírez¹, G. Leloudas^{5,2}, T. Zafar⁶, D. Malesani², and J. Hjorth²

¹ Instituto de Astrofísica de Andalucía (IAA-CSIC), Glorieta de la Astronomía s/n, E-18008, Granada, Spain
e-mail: adeugartepostigo@gmail.com

² Dark Cosmology Centre, Niels Bohr Institute, Juliane Maries Vej 30, Copenhagen Ø, D-2100, Denmark

³ Centre for Astrophysics and Cosmology, Science Institute, University of Iceland, Dunhagi 5, IS-107 Reykjavik, Iceland

⁴ University of Leicester, University Road, Leicester LE1 7RH, UK

⁵ The Oskar Klein Centre, Department of Physics, Stockholm University, 106 91 Stockholm, Sweden

⁶ Laboratoire d'Astrophysique de Marseille - LAM, Université Aix-Marseille & CNRS, UMR7326, 38 rue F. Joliot-Curie, 13388 Marseille Cedex 13, France

Received ; accepted

ABSTRACT

Context. The extreme brightness of gamma-ray burst (GRB) afterglows and their simple spectral shape make them ideal beacons to study the interstellar medium of their host galaxies through absorption line spectroscopy at almost any redshift.

Aims. We describe the distribution of rest-frame equivalent widths (EWs) of the most prominent absorption features in GRB afterglow spectra, providing the means to compare individual spectra to the sample and identify its peculiarities.

Methods. Using 69 low-resolution GRB afterglow spectra, we conduct a study of the rest-frame EWs distribution of features with an average rest-frame EW larger than 0.5 Å. To compare an individual GRB with the sample, we develop *EW diagrams* as a graphical tool, and we give a catalogue with diagrams for the 69 spectra. We introduce a *line strength parameter (LSP)* that allows us to quantify the strength of the absorption features in a GRB spectrum as compared to the sample by a single number. Using the distributions of EWs of single-species features, we derive the distribution of their column densities by a curve of growth (CoG) fit.

Results. We find correlations between the *LSP* and the extinction of the GRB, the UV brightness of the host galaxies and the neutral hydrogen column density. However, we see no significant evolution of the *LSP* with the redshift. There is a weak correlation between the ionisation of the absorbers and the energy of the GRB, indicating that, either the GRB event is responsible for part of the ionisation, or that galaxies with high-ionisation media produce more energetic GRBs. Spectral features in GRB spectra are, on average, 2.5 times stronger than those seen in QSO intervening damped Lyman- α (DLA) systems and slightly more ionised. In particular we find a larger excess in the EW of C IV $\lambda\lambda 1549$ relative to QSO DLAs, which could be related to an excess of Wolf-Rayet stars in the environments of GRBs. From the CoG fitting we obtain an average number of components in the absorption features of GRBs of $6.00^{+1.00}_{-1.25}$. The most extreme ionisation ratios in our sample are found for GRBs with low neutral hydrogen column density, which could be related to ionisation by the GRB emission.

Key words. Gamma-ray burst: general; Techniques: spectroscopic; Galaxies: ISM; Galaxies: high-redshift; dust, extinction

1. Introduction

Long gamma-ray burst afterglows (GRBs) shine, during the first hours, as the most luminous objects that can be detected in the Universe (Kann et al. 2007; Racusin et al. 2008). They have been observed at almost any redshift, from nearby (GRB 980425 was the nearest one, at $z = 0.008$, Galama et al. 1998) to the very distant Universe (GRB 090429B is the current record-holder with a photometric redshift of $z = 9.4$, Cucchiara et al. 2011, GRB 090423 being the furthest spectroscopically confirmed at $z = 8.2$, Tanvir et al. 2009; Salvaterra et al. 2009). Their optical spectra are normally well reproduced by a clean, simple power-law, making them ideal beacons to probe the material in the line of sight of the GRBs. Using optical spectroscopy it is possible to study the dust extinction, that introduces a curvature in the spectra (see e.g. Kann et al. 2010; Schady et al. 2010; Zafar et al. 2011), we can learn about intervening systems, located between the host galaxy of the GRB and the observer (Prochter et al. 2006; Tejos et al. 2007; Vergani et al. 2009) or about the material located within the host galaxy itself (Vreeswijk et al. 2007; D'Elia et al. 2009).

Most of the knowledge that we currently have about the interstellar medium (ISM) of GRBs comes from the study of individual events. However, as the samples of GRB afterglows become larger, much can be gained from statistical studies. This however, does not come without complications: Due to the very wide range of redshifts, very different rest-frame wavelength ranges are probed and tools need to be developed for their common study. Furthermore, the large samples of GRB afterglows are dominated by low resolution spectra. In these spectra, the line profiles cannot be fitted to derive column densities and the different components that form each feature cannot be resolved. This means that we can only measure equivalent widths (EW) of the lines, which limits the information that can be extracted from a single spectrum. However, we can attempt to derive some of the information contained in these spectra through the use of statistical analysis of large samples.

In this paper, we use 69 low resolution optical spectra to study the absorption features created by material within the GRB host galaxies. In particular we look at the distribution of the rest-frame EWs of the most prominent lines found in GRB afterglow spectra. Based on this, we devise observational tools to easily

evaluate the different types of environments that host GRBs and understand their properties and diversity.

The paper is structured as follows: Section 2 presents the sample, the methods used and the biases and limitations of our study, section 3 presents the results of the analysis, section 4 discusses the results and finally, section 5 gives our conclusions.

2. Sample and method

This work is based on the sample presented by Fynbo et al. (2009) selecting those spectra with known redshifts and a resolution $300 < R < 2000$, to have data of similar characteristics. The selection criteria of this sample, first proposed by Jakobsson et al. (2006b) and later refined by Fynbo et al. (2009) were chosen to achieve a high degree of completeness and to be as independent as possible of the optical properties of the afterglow: (1) burst duration longer than 2 s, (2) precise localisation, normally provided in X-rays by *Swift*/XRT, and distributed within 12 hr of the burst, to allow a rapid follow-up, (3) small Galactic extinction ($A_V < 0.5$ mag), (4) favourable declination for optical follow-up observations ($-70^\circ < \delta < +70^\circ$), and a distance between the sun and the field of more than 55° , to allow at least 1 hr of observations to secure spectroscopy.

We add 8 further low-resolution spectra to those presented by Fynbo et al. (2009), obtained after the publication but with similar criteria, as detailed in Appendix II of the online material. The total sample comprises 69 spectra. This includes 7 spectra that were part of the sample of Fynbo et al. (2009) but that did not meet all the criteria outlined in the previous paragraph.

This study analyses the distribution of rest-frame EWs, which is only possible for the most prominent absorption features in GRB afterglow spectra (the number of detections is still too small for faint features). Our sample is limited to those absorption features that have a rest-frame EW of at least 0.5 \AA in the composite spectrum presented by Christensen et al. (2011), which add to a total of 22 features. Some lines produced by transitions from excited fine structure and metastable states are known to vary during the evolution of the GRB and would introduce a further uncertainty in the results, so we exclude them from our analysis. Using the same argument, we exclude from our dataset the line at 2186.96 \AA that Christensen et al. (2011) identify as due to Mn I, as we believe that it is actually not due to this species but most probably to a transition from a fine structure line or a metastable state. This is supported by the fact that it is only seen in spectra with many other fine structure features and that it is detected only in early spectra. Furthermore, other Mn I lines that should have been simultaneously detected are not present in the composite spectrum.

We use the EW measurements provided by Fynbo et al. (2009), together with the 8 other unpublished spectra, and complement them with detection limits that we calculate for each feature in the individual spectra. To obtain the detection limits we use the individual spectra with their corresponding error spectra and measure the uncertainty at the location of the features over a wavelength span equivalent to the instrumental resolution, which is determined by the width of the slit (with this we assume that the lines are unresolved with our resolution, which is generally the case). The limits presented in this work are $3\text{-}\sigma$. We excluded from the analysis the regions of the spectra that were affected by strong telluric features. Tables 1 and 2 display the rest-frame EWs and limits for the lines in each spectrum.

2.1. EW histogram fitting

Using the data described above we build histograms of EWs in a logarithmic scale (see Fig. 1 for an example). To consider the EW uncertainties, we do not give all the weight of the measurement to a single bin, but instead we use a gaussian distribution to distribute the weight over the different bins according to the uncertainty of the measurement. For the detection limits, we distribute the weight evenly over all the possible values below the $3\text{-}\sigma$ limit in linear space.

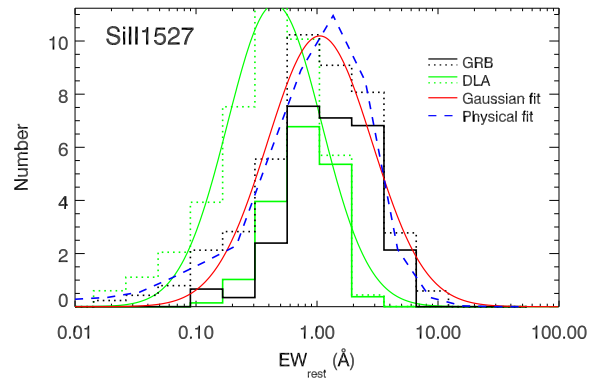


Fig. 1. EW distribution of the SiII feature at 1527 \AA . The thick black line histogram indicates only detections, whereas the dotted histogram includes also the limits. The red line is the best fit of the complete histogram with a lognormal distribution and the dashed blue line is a physical fit as described in Section 3.4. In green we show a histogram of EWs in a sample of DLA systems (see Section 3.3) and its lognormal fit. Similar histograms for all the lines in the sample can be found in Fig. B.1 of the online material.

In contrast with the work published by Christensen et al. (2011), where the EWs are weighted with the signal to noise ratio of the individual spectra to get a typical GRB spectrum, our aim is to study the actual distribution, independently of the signal to noise ratio of the spectra. To give a statistical value to the distributions that we obtain, as a first order approximation, we fit the histograms (detections plus limits) to a log-normal distribution. This gives us a typical EW value for the line and a standard deviation in the logarithmic space. The results of these fits are displayed in Table 3. The table includes also the number of detections and limits for each of the features in our sample. Figure 2 shows these results graphically, including information on the ionisation potential of each transition (see Table 4).

2.2. On the fitting function

In our study we assume that the column density of each individual species is described by a log-normal distribution. However, this does not directly imply that the distribution of EWs will also have a similar distribution. The column densities will be convolved with the curve of growth (CoG), distorting the original distribution. In this section we simulate the effect of a log-normal distribution convolved with typical CoG using Monte Carlo simulations.

Figure 3 shows how a log-normal histogram of column densities for Si II $\lambda 1527$ with $\log(N/\text{cm}^{-2}) = 14.5 \pm 1.0$ randomly generated (5000 tests) is transformed into a distribution of EWs. To do this, we also consider a random distribution of particle velocities following a log-normal distribution with

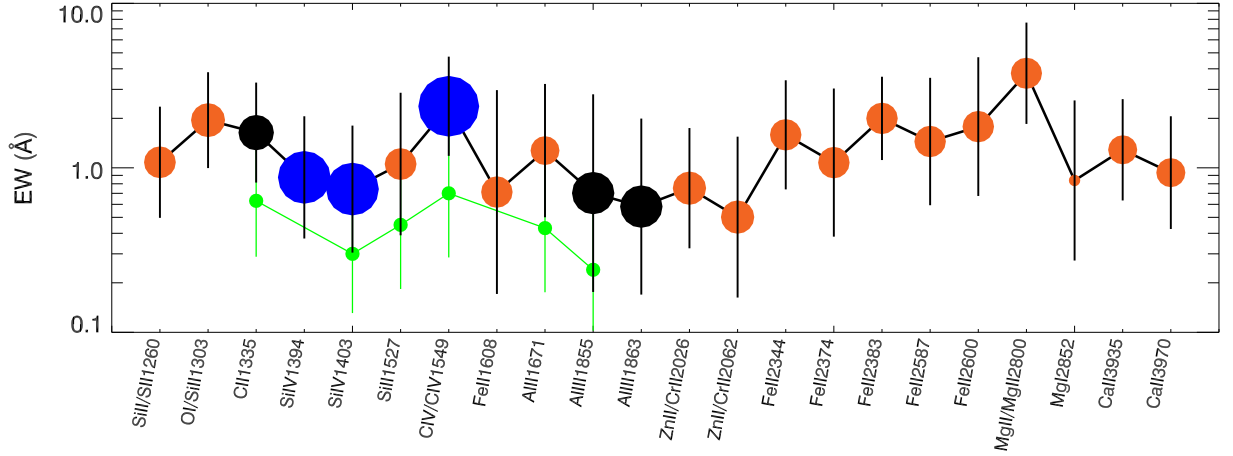


Fig. 2. Average strength of the different lines together with their standard deviation, as displayed in Table 3. The area of the dots are proportional to the ionisation potential of each species. We mark in orange the low ionisation lines (< 10 eV), in blue the high ionisation lines (> 30 eV) and in black the intermediate lines and the blend of O I/Si II $\lambda\lambda 1302, 1304$. In green we plot the average EWs for quasar intervening DLAs for a subsample of lines (see Sect. 3.3).

Table 3. Fits to the distribution of lines, including the number of detections and detection limits for each species. We show $10^{\langle \log EW \rangle}$ instead of $\langle \log EW \rangle$ as it allows a more intuitive interpretation.

Feature	Det.	Lim.	$10^{\langle \log EW \rangle}$ (Å)	$\sigma_{\log(EW/\text{Å})}$
Si II/S II $\lambda\lambda 1260, 1260$	15	20	1.08	0.34
O I/Si II $\lambda\lambda 1302, 1304^a$	22	15	1.95	0.29
C II $\lambda 1335^a$	23	16	1.64	0.30
Si IV $\lambda 1394$	19	19	0.88	0.37
Si IV $\lambda 1403$	19	19	0.74	0.39
Si II $\lambda 1527$	27	16	1.05	0.43
C IV $\lambda\lambda 1548, 1551$	35	7	2.37	0.30
Fe II $\lambda 1608$	19	24	0.71	0.61
Al II $\lambda 1671$	26	13	1.27	0.41
Al III $\lambda 1855$	15	27	0.70	0.60
Al III $\lambda 1863$	14	29	0.58	0.53
Zn II/Cr II $\lambda\lambda 2026, 2026$	16	27	0.75	0.37
Zn II/Cr II $\lambda\lambda 2063, 2062$	11	26	0.50	0.49
Fe II $\lambda 2344^a$	23	14	1.59	0.33
Fe II $\lambda 2374$	17	20	1.08	0.45
Fe II $\lambda 2383^a$	23	15	2.00	0.25
Fe II $\lambda 2587$	20	16	1.45	0.39
Fe II $\lambda 2600^a$	18	16	1.78	0.42
Mg II $\lambda\lambda 2796, 2803$	27	4	3.76	0.30
Mg I $\lambda 2852$	12	18	0.84	0.49
Ca II $\lambda 3935$	7	8	1.29	0.31
Ca II $\lambda 3970$	7	8	0.93	0.34

^a In some cases this line is blended with a fine structure transition of the same species. This can be significant in early spectra, as the fine structure line is normally excited by the prompt GRB emission.

$\log(b/\text{kms}^{-1}) = 1.1 \pm 0.3$ (equivalent to 12.6 km s^{-1}). We can see how, in the border between the linear and the saturated regime, where we find the features studied in this paper, the histogram has a tail to lower values of EWs and is truncated for high EWs due to the effect of saturation. This is similar to what we see in Fig. 1 and Fig. B.1 for most of the lines in our sample.

This implies that using log-normal distributions to fit the EW histograms is not an accurate physical description. However, due to the limited size of the sample, and the fact that the tail of the distribution towards low EWs is not well sampled in most of the

Table 4. Ionisation potential of the ionised species in our sample, from Morton (2003).

Species	Ionisation potential (eV)
Al II	5.99
Ca II	6.11
Mg II	7.65
Fe II	7.90
Si II	8.15
Zn II	9.39
C II	11.26
Al III	18.83
Si IV	33.49
C IV	47.89

cases (it is mainly populated by detection limits), we use the log-normal distribution as a first degree approximation. Furthermore, the use of such a simple fitting function allows us to perform an efficient and model independent observational analysis. In section 3.4 we attempt to use a more complex fit of the data to derive statistical distributions of column densities.

2.3. Biases and limitations

When using this sample, we must be aware that there are observational biases that limit the statistical value of the study, even if the data were obtained using criteria designed to minimise them. Within the sample criteria, there were cases for which a spectrum could not be obtained and/or the redshift was not constrained. These missing data will be dominated by faint afterglows, probably due to high extinctions, or by low density environments, which produce weaker features. The biases of this sample, which includes $\sim 1/3$ of the bursts meeting the observational criteria during the period of the study, are explained in detail by Fynbo et al. (2009).

For the spectra with a large amount of limits as compared to line detections, the way in which we treat the limits will affect our fits. We have chosen to give equal probability in the linear space to all the possible values below the $3\text{-}\sigma$ limits as this is the less model-dependent method.

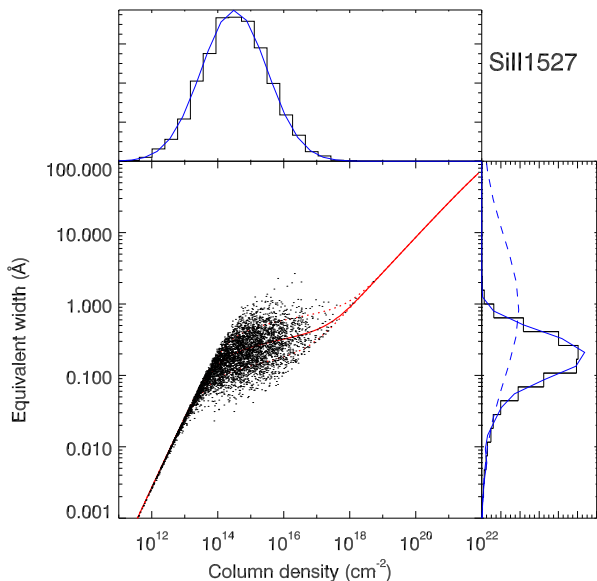


Fig. 3. Convolution of a log-normal distribution of column densities of Si II $\lambda 1527$, randomly generated, with a CoG to a distribution of EWs. We have assumed a distribution with $\log(N/\text{cm}^{-2}) = 14.5 \pm 1.0$ and also a log-normal distribution of particle velocities with $\log(b/\text{km s}^{-1}) = 1.1 \pm 0.3$ (equivalent to 12.6 km s^{-1}). The red continuous line indicates the CoG using the central b parameter, while the dotted lines are for b values $1-\sigma$ above or below. Continuous blue lines mark the distribution of column densities and its corresponding distribution of EWs once convolved with the CoG. The blue dashed line is the EW distribution that would be produced if the CoG would only have a linear regime.

On the other hand, there are limitations on the study of EWs in low resolution spectra as compared to determining the column densities of material with Voigt profile fitting in high resolution spectra. In most of the cases, the lines that we are studying are in the saturated regime, where the strength of the lines are not linearly related with the amount of material, so line ratios must be handled with care. In this sense, the study of the EWs of individual bursts can give us an idea of the environment within GRB host galaxies, but a quantitative description can be more challenging (see section 3.4).

Finally, one must be cautious when studying some of the individual features due to blending of several species. The most prominent case in our sample is the feature at 1303 \AA produced by the blend of O I $\lambda 1302.17$, Si II $\lambda 1304.37$ and O I* $\lambda 1304.86$. Both O I $\lambda 1302.17$ and Si II $\lambda 1304.37$ are intense features that cannot be disentangled at our resolution and that add similar contributions, whereas O I* $\lambda 1304.86$ is only important in some very early spectra. In a similar way the two Zn II features are blended with Cr II. Although in most cases the Zn II is dominant, the contribution of Cr II cannot be neglected. In the case of early spectra, some Fe II features as well as C II can be blended with fine structure transitions of the same species. These fine structure transitions can be induced by the radiation from the prompt GRB emission and in consequence have an EW that can vary with time. These features are disregarded in the physical fit performed in Sect. 3.4. In Table 3 we indicate the lines that are affected by blends with other lines.

3. Results

3.1. EW diagrams

By comparing an individual spectrum with the sample of EW distributions, one can understand the general characteristics of the GRB environment. To do this in an effective way, we create comparative *EW diagrams*, where the EWs of an individual burst are plotted together with the average and standard deviations of the sample, which are the same as shown in Fig. 2 (See Fig. 4 for some examples and Fig. C.1 of the online material for the complete catalogue of EW diagrams).

These diagrams are useful to quickly estimate the strength of the absorption features as compared to the sample as well as to identify environments with unusual characteristics. Independently of the strength of the features, the relative line strengths should be similar to the sample average if the composition of GRB host galaxies is uniform. An EW diagram that does not follow the shape of the average diagram (see the 3 bottom panels of Fig. 4), immediately tells us that the environment of the GRB has peculiarities. As an example, GRB 060526, second from the bottom of Fig. 4, shows very low EWs for highly ionised species, such as Si IV, C IV or Al III as compared to their lower ionised transitions Si II, C II and Al II. For GRB 070411 the behaviour is the opposite.

As EW diagrams can easily reveal anomalous feature strengths, they are also a useful tool to identify faulty measurements, features that are affected by contamination of intervening material, artefacts in the data, etc. In fact, while writing this paper we have identified several such cases, allowing us to revise the data and, when possible, correct the measurements.

3.2. Line Strength Parameter

Comparative studies of spectra over a wide range of redshifts can be a difficult task, as the spectral features can fall at very different wavelengths in the observer frame. To study the line strengths of the different bursts, independently of the wavelength range covered, we define the *line strength parameter* (*LSP* hereafter) as:

$$LSP = \frac{1}{N} \sum_{i=1}^N \frac{\log EW_i - \langle \log EW \rangle_i}{\sigma_{\log EW_i}}, \quad (1)$$

where EW_i is the equivalent width for each of the individual detected lines in the spectrum, $\langle \log EW \rangle_i$ the central equivalent width obtained from the fits in Sect. 3, $\sigma_{\log EW_i}$ is the standard deviation (both shown in Table 3) and N the total number of lines used to calculate the *LSP*.

This parameter measures the strength of the absorption features of a spectrum as compared to the average GRB spectrum. A value of zero would mean that the absorption features in the spectrum have the same strength as the average spectrum. Positive values indicate bursts with stronger than average lines, and equal to 1.0 if the deviation is equivalent to $1-\sigma$. In the same way a negative value implies weak lines. In Table 5 we display the *LSP* for each of the GRBs considered in the sample. We also calculate the standard deviation (of the summation values in Eq. 1) for each of the GRBs that indicates how different is the distribution of line strengths with respect to the average of GRBs. In the case of a spectrum where we only have detection limits, we use the strongest limit given by a single line to calculate a limit value for the *LSP*.

The distribution of *LSPs* can be fitted by a gaussian with an average value of $\langle LSP \rangle = -0.03$ and a standard deviation

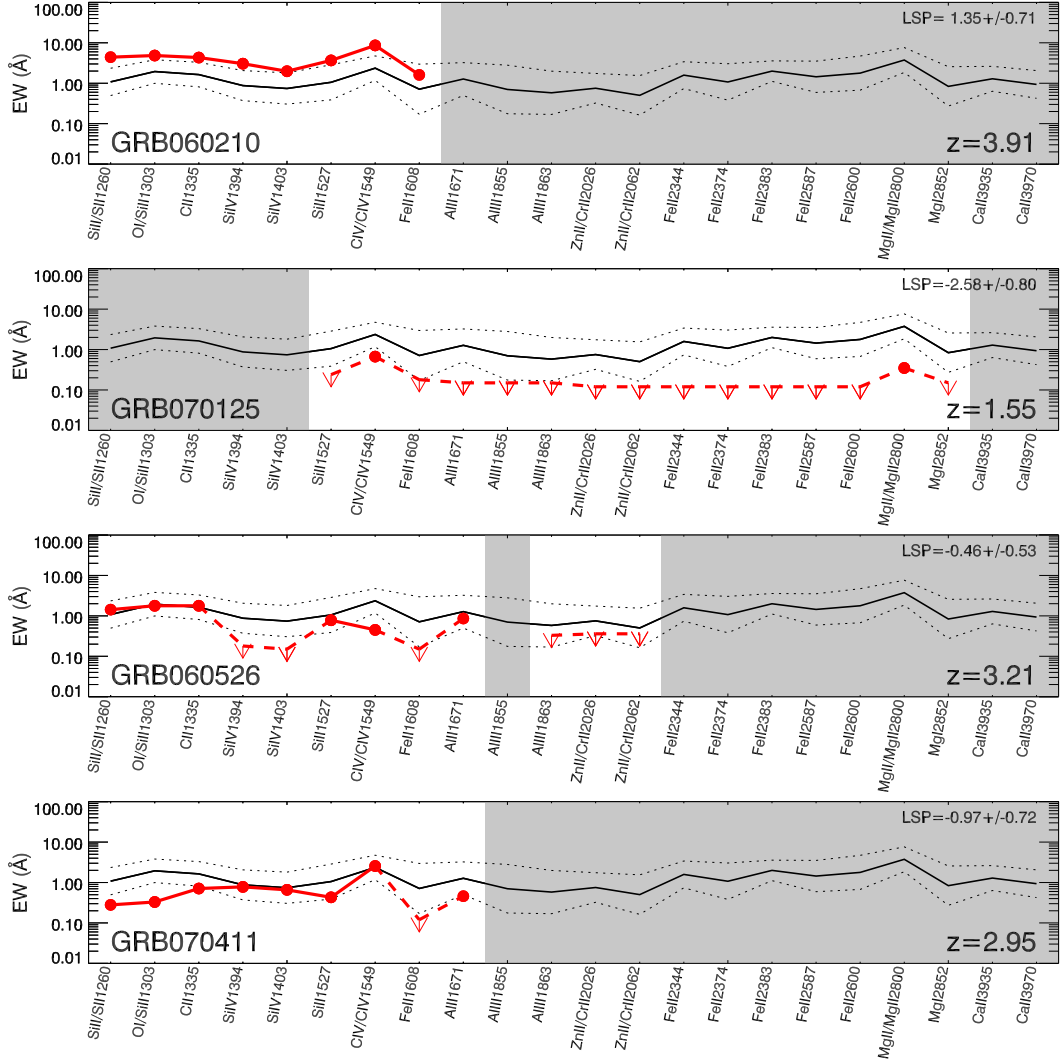


Fig. 4. EW diagrams: In red we represent the EWs of the spectral features if each afterglow spectrum. The continuous black line is the average of the sample of GRBs (see Fig. 2), whereas the dotted lines indicate the standard deviations over and under this value. Gray regions mark the range where there is no spectral coverage or it is affected by strong telluric features. Each panel shows examples of individual bursts: GRB 060210, an afterglow with strong lines; GRB 070125, with weak features; GRB 060526, with a very weakly ionised environment; GRB 070411, with very high ionisation.

of $\sigma_{LSP} = 0.72$. The average LSP is not centred on zero but slightly below, as the distribution of EWs is not fitted by a perfect gaussian but has a tail towards lower values (see Sect. 2.2). These values can be used to calculate the percentile of line strength that corresponds to a specific afterglow (see Fig. 5) through the following formula:

$$P_{LSP,i} = 50 \left(1 + \text{ERF} \left(\frac{LSP_i - \langle LSP \rangle}{\sqrt{2}\sigma_{LSP}} \right) \right) \quad (2)$$

To extract further information, we calculate two additional LSP s, separately using just high-, or low-ionised species. In this way we can see if the behaviour is different for high ionisation and low ionised environments. The higher ionisation lines could be more closely associated with star forming regions, such as the ones that produce GRBs, whereas the lower ionisation species would be more representative of the overall galaxy. For the low-ionisation LSP we use the lines of species with ionisation potential lower than 10 eV and for the high-ionisation LSP those that have potentials higher than 30 eV, as shown in Table 4. Both

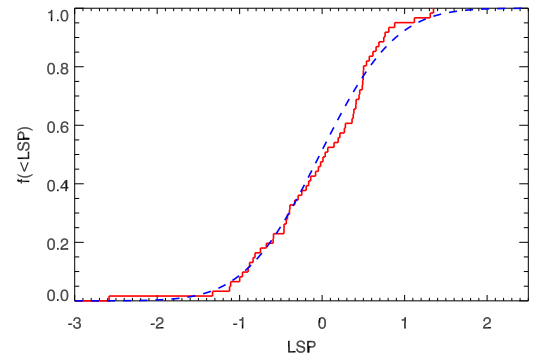


Fig. 5. Cumulative distribution of the line strength parameter. The red line are the observations, whereas the the blue dashed line is the best fit to a gaussian distribution.

Table 5. Neutral hydrogen column density, derived from Ly α , LSP, low-ionisation LSP and high-ionisation LSP for the 69 spectra in our sample.

GRB	$\log N_{\text{HI}}$	LSP	LSP _L	LSP _H
050319	20.90±0.20	0.69±0.30	0.67±0.14	1.20±0.25
050401	22.60±0.30	0.57±0.46	0.34±0.31	0.12±0.03
050408	—	0.49±0.37	0.34±0.22	—
050730	22.10±0.10	-0.46±0.27	-0.48±0.22	-0.31±0.12
050802	—	0.41±0.18	0.48±0.18	0.20±0.04
050824	—	-0.68±0.24	-0.68±0.24	—
050908	17.60±0.10	-1.12±0.96	< -3.19	0.09±0.11
050922C	21.55±0.10	-0.90±0.57	-0.64±0.26	-0.75±0.27
060115	21.50±0.10	0.01±0.22	0.28±0.06	-0.84±0.18
060124	18.50±0.50	0.28±0.08	< -1.55	0.28±0.08
060206	21.85±0.10	0.50±0.15	< 1.01	—
060210	21.55±0.15	1.35±0.71	1.21±0.47	1.48±0.53
060502A	—	-0.16±0.21	-0.16±0.21	—
060526	20.00±0.15	-0.46±0.53	-0.12±0.14	-2.39±0.51
060614	—	< -0.37	< -0.37	—
060707	21.00±0.20	0.36±0.35	0.66±0.20	-0.87±0.19
060714	21.80±0.10	0.62±0.33	0.52±0.25	0.64±0.23
060729	—	-0.84±0.40	-0.84±0.40	—
060904B	—	0.04±0.13	0.04±0.13	—
060906	21.85±0.10	-0.42±0.19	-0.31±0.07	-0.29±0.06
060908	—	0.45±0.10	< -0.18	0.45±0.10
060926	22.60±0.15	-0.25±0.09	-0.10±0.02	-0.32±0.07
060927	—	< 0.23	< 0.23	—
061007	—	0.65±0.34	0.65±0.34	—
061021	—	-1.00±0.21	-1.00±0.21	—
061110A	—	-0.05±0.01	-0.05±0.01	—
061110B	—	0.14±0.24	-0.37±0.11	0.64±0.19
061121	—	0.76±0.37	0.79±0.43	0.90±0.19
070110	21.70±0.10	-0.33±0.41	-0.09±0.20	-0.95±0.35
070125	—	-2.58±0.80	-3.35±0.71	-1.82±0.39
070306	—	< 0.36	< 0.36	< 1.69
070318	—	-0.39±0.37	-0.39±0.37	—
070411	19.30±0.30	-0.97±0.72	-1.24±0.46	-0.05±0.05
070419A	—	-0.29±0.12	-0.29±0.12	—
070506	22.00±0.30	0.50±0.39	0.54±0.28	0.70±0.28
070508	—	< 0.39	< 0.39	—
070611	—	-0.81±0.17	-0.81±0.17	< -1.84
070721B	21.50±0.20	0.27±0.24	0.17±0.04	0.56±0.21
070802	21.50±0.20	1.12±0.68	1.35±0.68	-0.16±0.03
071020	—	0.50±0.28	0.50±0.28	< -0.13
071031	22.15±0.05	-0.40±0.32	-0.47±0.30	0.02±0.04
071112C	—	-0.59±0.32	-0.59±0.32	—
080210	21.90±0.10	0.22±0.32	0.02±0.20	0.62±0.22
080319B	—	-0.75±0.23	-0.75±0.23	—
080319C	—	0.46±0.24	0.45±0.10	0.60±0.13
080330	—	-0.43±0.42	-1.12±0.34	-0.47±0.10
080411	—	-0.08±0.12	-0.15±0.11	—
080413B	—	0.19±0.28	0.44±0.22	—
080520	—	< -0.60	< -0.60	< 2.11
080603B	21.85±0.05	-1.11±0.59	-1.57±0.48	-0.83±0.30
080604	—	0.38±0.21	0.38±0.21	—
080605	—	0.54±0.45	0.61±0.36	1.11±0.24
080607	22.70±0.15	0.88±0.47	0.80±0.30	1.06±0.38
080707	—	0.49±0.28	0.49±0.28	—
080710	—	-1.33±0.70	-1.33±0.70	—
080721	21.60±0.10	0.41±0.31	0.52±0.24	0.52±0.22
080810	—	-0.19±0.19	-0.79±0.17	0.40±0.09
080905B	—	-0.02±0.32	-0.06±0.25	-0.51±0.11
080913	—	< -0.42	< -0.42	—
080916A	—	0.38±0.08	0.38±0.08	—
080928	—	-0.88±0.62	-0.98±0.62	-0.16±0.03
081007	—	< 3.43	< 3.43	—
081008	21.59±0.10	-0.59±0.40	-0.30±0.15	-0.83±0.31
090102	—	0.75±0.49	0.87±0.50	0.56±0.12
090516	21.73±0.10	1.31±0.64	1.25±0.44	1.21±0.43
090519	—	< -0.55	< 0.50	< -0.55
090529	—	0.07±0.17	0.61±0.13	-0.47±0.10
090812	22.30±0.10	-0.14±0.35	-0.07±0.21	-0.65±0.26
090814A	—	0.81±0.34	0.81±0.34	—

low-ionisation LSP (LSP_L) and high-ionisation LSP (LSP_H) are displayed in Table 5.

3.3. Comparison with quasar DLAs

In general, GRBs are produced in environments with large amounts of neutral gas, with neutral hydrogen column densi-

ties that lie in the damped Lyman- α (DLA) regime. In this section we measure the rest-frame EWs of a sample of intervening DLA systems in quasar spectra in a similar way to what we have done for GRBs. We have used the original QSO-DLA sample from Noterdaeme et al. (2009) based on the Sloan Digital Sky Survey Data Release 7 (SDSS-DR7) database of QSO spectra. These authors automatically searched for DLA lines, refining their Ly α fits whenever metal lines are detected redward of the Ly α forest. We have selected all systems from their list with $\log(N_{\text{HI}}/\text{cm}^{-2}) > 20$ and redshifts in the range $2.2 < z < 3.2$, located at least 5000 km s^{-1} from a background QSO with $R < 21$. To simplify the analysis we have limited the comparison to the following spectral features: C II λ 1335, Si IV λ 1403, Si II λ 1527, C IV λ 1549, Al II λ 1671 and Al III λ 1855.

In Fig. 1 and Fig. C.1 of the Appendix we show the histograms of the EWs for GRBs and in the cases of the lines where we have DLA data, we also represent additional histograms with DLA data in green. The DLA histograms have been scaled down to match the smaller number of GRBs so that the histograms can be plotted together. Similar measurements to the ones displayed in Table 3 are given for DLAs in Table 6. It is immediately clear that the features produced by quasar intervening DLAs are weaker. We find that the EWs of GRB absorption features are, on average, 2.5 ± 0.6 times larger than the DLAs. The excess of material in the line of sight of GRBs as compared to DLAs has been already described (Savaglio et al. 2003; Jakobsson et al. 2006a) and is interpreted as due to the different impact parameters: The material generating the DLA absorptions are produced as the line of sight to the quasar intercepts the intervening galaxy, which is statistically more probable to happen in the outskirts of the galaxy (Prochaska et al. 2007; Fynbo et al. 2008; Pontzen et al. 2010). On the other hand, GRBs are produced inside the most luminous regions (Bloom et al. 2002; Fruchter et al. 2006; Svensson et al. 2010) of star forming galaxies (Christensen et al. 2004), implying that the light will have to interact with much more material before escaping the host galaxy. However, we note that all the lines in our DLA sample are between 2.3 and 2.9 times weaker than the ones in the GRB sample except for one. In the case of C IV, the GRB lines are 3.4 times stronger than those found in DLAs. This excess of C IV could be indicative of an excess of Wolf-Rayet stars (Berger et al. 2006) in the GRB host galaxies, as compared to QSO DLAs.

For comparison, we have plotted, in Fig. 2, the average EWs measured for DLAs (in green) together with the values for GRBs.

Table 6. Fits to the distribution of lines for quasar intervening DLA systems.

Feature	$10^{\langle \log \text{EW} \rangle}$ (Å)	$\sigma_{\log(\text{EW}/\text{Å})}$
C II λ 1335	0.63	0.34
Si IV λ 1403	0.30	0.36
Si II λ 1527	0.45	0.39
C IV λ 1548,1551	0.70	0.39
Al II λ 1671	0.43	0.39
Al III λ 1855	0.24	0.37

3.4. Physical fit of the EW distributions

In this section we attempt to fit the distributions of EWs that we have obtained, using CoGs to derive the actual distribution of

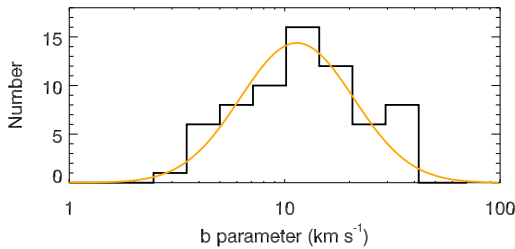
Table 7. Distribution of column densities derived from the EWs. From the fits we derive that the average number of line components is $6.00^{+1.25}_{-1.00}$.

Species	Features (Å)	$\langle \log(N/cm^{-2}) \rangle_{comp}$	$\sigma_{\log(N/cm^{-2})}$	$\langle \log(N/cm^{-2}) \rangle_{total}$
Si II	1527	$14.50^{+0.28}_{-0.28}$	$1.10^{+0.30}_{-0.30}$	$15.28^{+0.28}_{-0.28}$
Si IV	1394, 1403	$13.80^{+0.21}_{-0.21}$	$0.80^{+0.30}_{-0.30}$	$14.58^{+0.21}_{-0.21}$
C IV	1549	$14.50^{+0.28}_{-0.21}$	$0.80^{+0.30}_{-0.30}$	$15.28^{+0.28}_{-0.21}$
Fe II	1608, 2374, 2587	$14.29^{+0.35}_{-0.35}$	$1.00^{+0.30}_{-0.30}$	$15.07^{+0.35}_{-0.35}$
Al II	1671	$13.38^{+0.28}_{-0.35}$	$1.20^{+0.30}_{-0.30}$	$14.16^{+0.28}_{-0.35}$
Al III	1855, 1863	$13.17^{+0.28}_{-0.28}$	$0.90^{+0.30}_{-0.30}$	$13.95^{+0.28}_{-0.28}$
Mg I	2852	$12.19^{+0.21}_{-0.21}$	$0.80^{+0.30}_{-0.20}$	$12.97^{+0.21}_{-0.21}$
Mg II	2800	$13.59^{+0.28}_{-0.28}$	$0.60^{+0.40}_{-0.40}$	$14.37^{+0.28}_{-0.28}$
Ca II	3935, 3970	$12.54^{+0.21}_{-0.21}$	$0.50^{+0.40}_{-0.20}$	$13.32^{+0.21}_{-0.21}$

column densities of each species. We use only features that are produced by single species (we exclude the O I/Si II, Zn II/Cr II and Si II/S II line blends, as well as the C II and Fe II that can be blended with fine structure lines, but we include doublets of the same species such as C IV, Mg I).

The fit is determined from the distribution of EWs of all the features simultaneously. To do this, we must make some assumptions: (1) The distribution of column densities is described by a log-normal distribution (characterised by $\langle \log N \rangle$ and $\sigma_{\log N}$). (2) The distribution of particle velocities is described by a log-normal distribution (characterised by $\langle \log b \rangle$ and $\sigma_{\log b}$). (3) The material producing the features is located in a series of clumps, the same for all the species, this will create a specific number of components.

To limit the amount of free parameters we will assume that the distribution of particle velocities has $\langle \log(b/km s^{-1}) \rangle = 1.1$ (equivalent to $12.6 km s^{-1}$) and $\sigma_{\log(b/km s^{-1})} = 0.3$. This is estimated from the values derived from line profile fitting in 10 GRB afterglows (with a total of 66 velocity components) observed with high spectral resolution using UVES at the Very Large Telescope (see Fig. 6, D’Elia et al. 2007; Piranomonte et al. 2008; Fox et al. 2008; D’Elia et al. 2009).

**Fig. 6.** Distribution of the b parameter for absorption components, measured by fitting voigt profiles in high-resolution spectra of GRB afterglows. The orange line is the log-normal fit.

The fitting code that we have created compares the EW histograms to models created in a similar way to what was shown in section 2.2. The models are computed for varying column density distributions and varying number of components. The method searches for minimum χ^2 values within an allowed range of parameters.

To simultaneously use as much information as possible, we fit all the features that we have in our sample together. The results of the fits are displayed in Table 7. The distributions giving

the best fits, obtained by this method are shown in Fig. 1 and Fig. C.1 as dashed blue lines. From these results we obtain that the typical number of components generating absorption lines is $6.00^{+1.25}_{-1.00}$. Within our sample, the most abundant species that are detected in the host galaxies of GRBs are C IV and Si II, with Ca II and Mg I being the least common.

4. Discussion

4.1. Ionisation ratios

Using the elements of our sample that have different states of ionisation, we can derive equivalent width ratios that will give indicative measures of the typical degrees of ionisation of each element in GRB host galaxies. This can be used to compare with the environments probed in quasar intervening DLA systems or to identify peculiar GRB environments that depart from the typical values.

We first compare Si IV $\lambda 1403$ with Si II $\lambda 1527$. These two lines have the advantage of being separated by only 124 Å in the rest-frame, so that they are normally covered in a single spectrum. Figure 7 shows the values of Si IV $\lambda 1403$ vs. Si II $\lambda 1527$ for both GRBs (red dots) and QSO intervening DLAs (green squares). The average ratio of the detections (limits are not considered here) are shown with a dashed line (red for GRBs, green for DLAs), and dotted lines represent the standard deviations. At a first glance we see that GRBs seem to have higher ratios of Si IV $\lambda 1403$ /Si II $\lambda 1527$. However, when we plot the ratio of the distributions from Table 3 (dashed-dotted line), where limits are considered, we see that it lies below the average value and that it is almost identical to the one from intervening DLAs. In the case of the DLAs the average value of the detections and the distribution are consistent. This implies that the previous average value is biased by non-detections of Si IV $\lambda 1403$, which is usually weaker than Si II $\lambda 1527$. This does not seem to be so significant for the DLA systems, as the two ratios match.

The ratio between C IV $\lambda 1549$ and C II $\lambda 1335$ can be a better estimator of the ionisation as, being both very strong features, it provides a large number of detections (Fig. 8). Furthermore, among the ionisation ratios given here, this one has the lowest dispersion in strength of the features, making the ionisation outliers stand out more clearly. Finally, the ionisation potential of C IV is the highest of our sample (see Table 4). In this case the average ratios of the detections and the ratio of the distribution average are consistent, meaning that the detection limits are not strongly affecting the results.

In the case of the Al III $\lambda 1855$ and Al II $\lambda 1671$ ratio, the ionisation potentials are not as extreme as in the previous cases, mean-

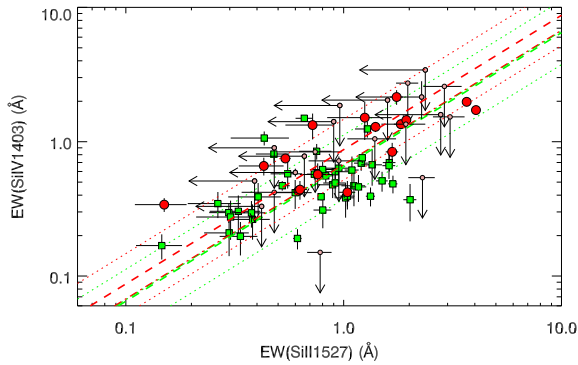


Fig. 7. Si $\text{IV} \lambda 1403$ vs. Si $\text{II} \lambda 1527$. Red dots are from GRB spectra whereas green boxes are from quasar intervening DLA systems. For clarity, detection limits are only plotted for GRBs. Dashed lines are the average values of the line ratios (detection limits are ignored), dotted are the standard deviation of these values and dashed-dotted lines are the ratios of the average values of the distributions. See Table 8 for a summary of the line ratios.

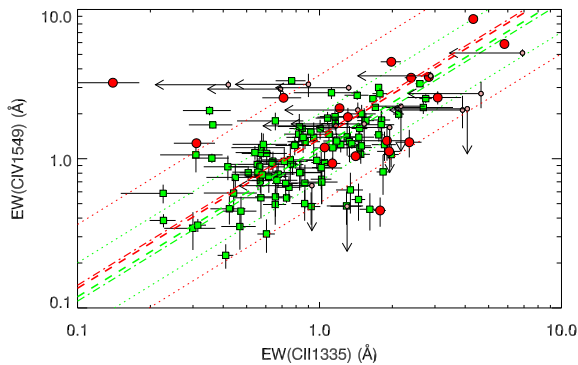


Fig. 8. C $\text{IV} \lambda 1549$ vs. C $\text{II} \lambda 1335$. The colour coding is the same as in Fig. 7.

ing that moderate star formation can account for the excitation of Al to these levels (see Fig. 9).

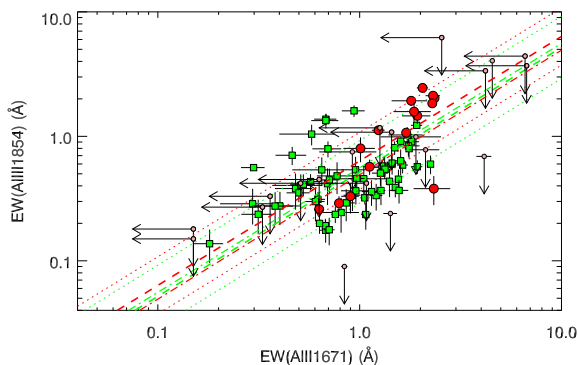


Fig. 9. Al $\text{III} \lambda 1855$ vs. Al $\text{III} \lambda 1671$. The colour coding is the same as in Fig. 7.

In Fig. 10 we plot the ratio of the two more extreme ionised species in our sample, C $\text{IV} \lambda 1549$ and Si $\text{IV} \lambda 1403$. Berger et al.

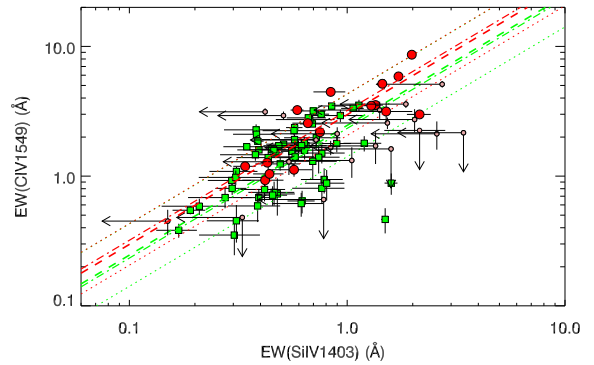


Fig. 10. C $\text{IV} \lambda 1549$ vs. Si $\text{IV} \lambda 1403$. The colour coding is the same as in Fig. 7.

(2006) suggest that a Wolf-Rayet outflow model would produce absorbers rich in carbon and low in silicon, making the C IV /Si IV a good tracer these kind of massive stars. In fact, this ratio shows a more significant difference with the DLA systems. This indicates a possible excess of Wolf-Rayet stars in the environments of GRBs, consistent with the models that explain long GRBs as the collapse of massive stars.

The fits to all these line ratios are given in Table 8.

Table 8. EW ratios of selected lines for GRBs and DLAs. Both the average of the detections (when both lines are detected) and the distributions (ratio of the average of the distributions from Tables 3 and 6) are shown. In the case of the average ratios of detections we give also the dispersion of the distribution.

Ratio	GRB		DLA	
	Det. Centre, σ	Dist. Centre	Det. Centre, σ	Dist. Centre
$\log \left(\frac{\text{Si IV } \lambda 1403}{\text{Si II } \lambda 1527} \right)$	-0.06, 0.23	-0.15	-0.19, 0.24	-0.18
$\log \left(\frac{\text{C IV } \lambda 1549}{\text{C II } \lambda 1335} \right)$	0.13, 0.43	0.16	0.07, 0.23	0.05
$\log \left(\frac{\text{Al III } \lambda 1855}{\text{Al III } \lambda 1671} \right)$	-0.20, 0.23	-0.26	-0.29, 0.25	-0.25
$\log \left(\frac{\text{C IV } \lambda 1549}{\text{Si IV } \lambda 1403} \right)$	0.47, 0.16	0.51	0.39, 0.24	0.37

Finally we plot both the ionisation ratios (EW of the highest-ionised species over the EW of the lowest-ionised species) of carbon and silicon in Fig. 11. The ratios of both C and Si allow us to easily separate highly-ionised (at the top right of the figure) and low-ionised environments (at the lower left) from the average values found in GRBs (centre). It is curious to see that the 4 GRBs with highest ionisation, GRBs 050908, 060124, 080810 and 070411 all have very low neutral hydrogen column densities, with $\log(N_{\text{H I}}/\text{cm}^{-2}) < 20$ (see also Sect. 4.2.3). This relation between high ionisation environments and low column density of neutral hydrogen was already noted by Jakobsson et al. (2006a) and later modelled by Thöne et al. (2011). In these very ionised spectra, the photons emitted by the GRB itself or of an environment rich in Wolf-Rayet stars would ionise the hydrogen. In the case of GRB 090426, the amount of absorbing H I was seen to decrease during the hours that followed the GRB (Thöne et al. 2011), supporting the hypothesis of the ionising GRB.

On the other side, bursts like GRBs 060526 and 060707 show very low ionisation. Given that GRBs are supposed to happen in strong star forming regions, we would expect ionised en-

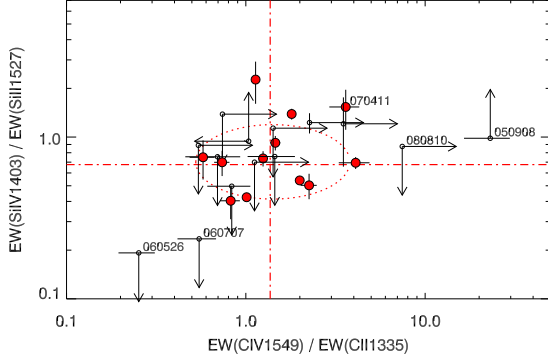


Fig. 11. Comparison between the ionisation ratio of carbon and silicon. Dashed dotted lines mark the average values of each ratio and the dotted ellipse the $1\text{-}\sigma$ area.

vironments. As a consequence, these bursts with very low ionisation might be mostly probing material that is in the line of sight but unrelated to the star forming regions where GRBs are produced.

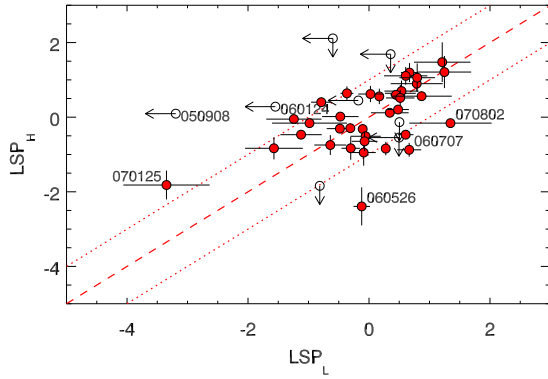


Fig. 12. Comparison of the high- and low-ionisation LSP s. The dashed line indicates equal low- and high-ionisation LSP . The dotted lines mark where they differ by 1.0.

Many GRBs cannot be included in plots like the one in Fig. 11 because of the lack of several of the species in the spectrum. In these cases we can study the ionisation of the GRB environment by using the LSP_L and LSP_H . Fig. 12 compares them and shows how some extreme environments, with very low or very high ionisation levels stand out.

4.2. LSP correlations

In the following paragraphs we study correlations (or the lack of them) between the strength of the absorption features (through the LSP) and several properties of the GRB and its host galaxy environment. For each case we use parametric (Pearson's r correlation coefficient) and non-parametric tests (Spearsman's ρ) to determine the strength of the correlations.

4.2.1. LSP vs. Observation time

As a first check, we study how the LSP correlates with the time after the GRB (rest frame) in which the observation was per-

formed. Christensen et al. (2011) find a decrease in the strength of several absorption features of our sample when they compare two composite spectra with average times of 0.4 and 5 hr after the burst. Our data shows no significant correlation of the LSP with time, as shown in Fig. 13. We find correlation coefficients of $r = -0.015$ (for a sample of 65 data points) and $\rho = -0.03$, implying a probability of correlation of 0.21 (0.3σ).

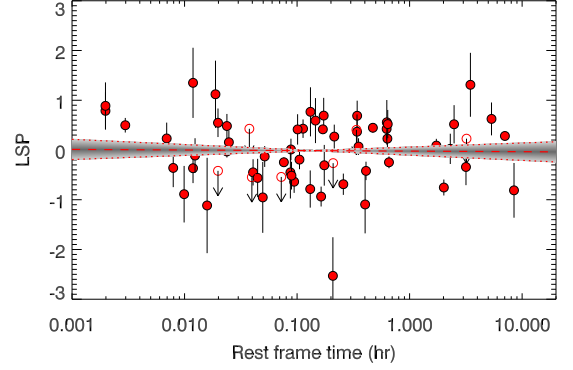


Fig. 13. Comparison of the LSP with the time of the observation in rest frame, showing no correlation. The shaded region indicates the uncertainty in the slope of the linear fit.

4.2.2. LSP vs. Extinction

We here compare the LSP with the extinction, parametrized by A_V , the equivalent extinction in the rest-frame V -band. A_V is usually derived from SED fitting of power-laws with a superposed extinction law. When available, we use the extinction determined by Zafar et al. (2011), using Kann et al. (2010) and Schady et al. (2010) for other cases.

When a GRB is seen through more material in its host galaxy, the absorption features in the spectrum show higher EWs. Furthermore, if the presence of this material is correlated with the presence of dust, the spectrum would also be more extinguished. This is precisely what we see in Fig. 14 where the LSP increases with increasing extinction. We obtain correlation coefficients of $r = 0.52$ (for a sample of 36 data points) and $\rho = 0.63$, indicating a probability of correlation of 0.99997 (3.7σ). A linear fit to the data gives $LSP = (0.98 \pm 0.28)A_V + (0.59 \pm 0.20)$.

4.2.3. LSP vs. $N_{H,O}$

As the amount of material producing the absorption features increases in the line of sight, together with the increase of the LSP , we would expect to see an increase in the column density of neutral hydrogen, measured through the fitting of the absorption Ly α feature.

Figure 15 (top) plots the LSP as a function of the Ly α -derived column density of neutral hydrogen, $N_{H,O}$ (from Fynbo et al. 2009). Unfortunately, this is only possible to measure from the ground for GRBs with redshift larger than $z \sim 2$, when the 1215 Å feature is redshifted into the visible range. Although there is some tendency to find higher N_H in large LSP spectra, there is a great dispersion, pointing to a large dispersion in the metallicities of GRB environments or independent regions generating the absorptions. Correlation coefficients of $r = 0.32$ (for a sample of 27 data points) and

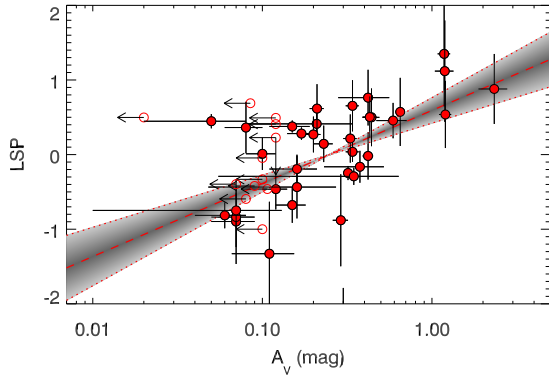


Fig. 14. Correlation between the $LS P$ and the intrinsic extinction of the GRB. The shaded region indicates the uncertainty in the slope of the linear fit.

$\rho = 0.15$, with a probability of correlation of 0.56 (0.7σ) confirms the weakness of the correlation. A linear fit to the data gives $LS P = (0.19 \pm 0.11) \log(N_{H1,0}/\text{cm}^{-2}) - (3.98 \pm 2.39)$. However, we note that the fit is constrained by those GRBs with $\log(N_{H1}/\text{cm}^{-2}) < 20$. If we exclude those bursts the fit is unconstrained.

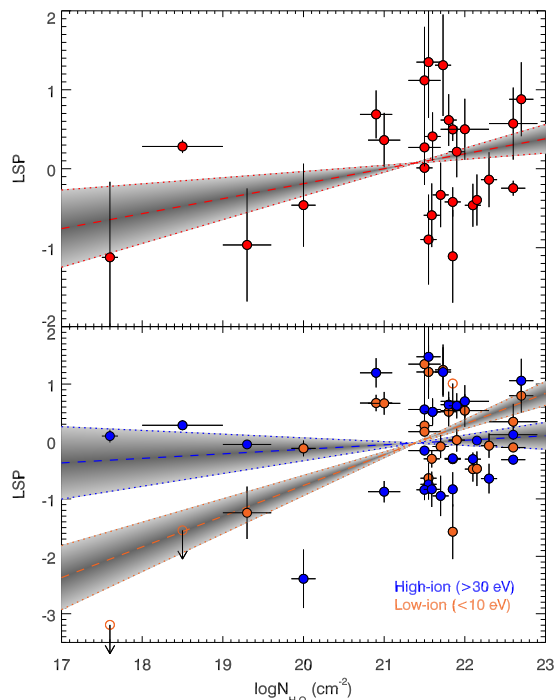


Fig. 15. Relation between the $LS P$ and the $\text{Ly}\alpha$ -derived N_H of the GRB. The shaded regions indicate the uncertainty in the slopes of the linear fits.

It is interesting to see how the plot changes when we consider separately the $LS P_L$ and $LS P_H$. Figure 15 (bottom) shows that GRBs with column densities $\log(N_{H1,0}/\text{cm}^{-2}) < 20$ present extreme ionisation states, showing predominantly very highly ionised environments, although there is also the case of a very low ionised burst. The relation of low neutral hydrogen column densities and high-ionisation has been already seen be-

fore (Jakobsson et al. 2006a; Campana et al. 2010; Thöne et al. 2011) and interpreted as due to the ionisation of hydrogen in the near GRB environment (Lazzati et al. 2001; Watson et al. 2007).

4.2.4. $LS P$ vs. $N_{H,X}$

Using X-ray measurements we can also obtain an estimate of the column density of neutral hydrogen ($N_{H,X}$) by fitting the spectrum of the X-ray afterglow with a power law and an extinction curve (Campana et al. 2010). However, this extinction is not directly caused by hydrogen but by metals, so it is very dependent on the composition of the host galaxy. The relation between the extinction and N_H is well known for the Milky Way, but the uncertainty is large in GRB host galaxies (Watson & Jakobsson 2012). Comparing the $LS P$ with the X-ray derived N_H (Fig. 16) shows a correlation but with large dispersion. We obtain correlation coefficients of $r = 0.39$ (for a sample of 44 data points) and $\rho = 0.40$, indicating a probability of correlation of 0.993 (2.6σ). A linear fit gives $LS P = (0.48 \pm 0.17) \log(N_{H,X}/\text{cm}^{-2}) - (10.51 \pm 3.74)$. In this case we find no significant difference when considering the low- and high-ionised $LS P$ s.

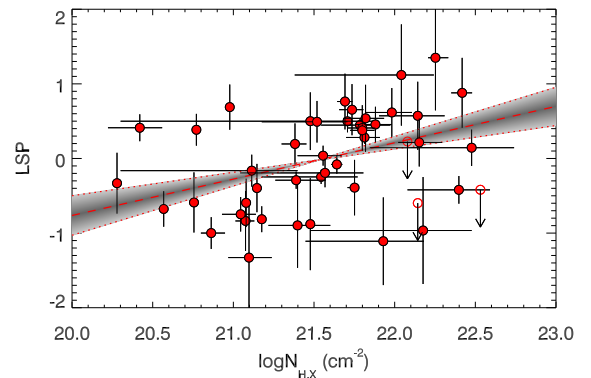


Fig. 16. Correlation between the $LS P$ and the X-derived N_H of the GRB. The shaded region indicates the uncertainty in the slope of the linear fit.

4.2.5. $LS P$ vs. Redshift

Thanks to the very broad redshift distribution of GRBs, they can help to answer questions related to the evolution of galaxies and their star formation history. In this section we look for a possible evolution of the $LS P$ with the redshift. Figure 17 shows a large dispersion in the $LS P$ s but no significant evolution. A linear fit to the dataset returns a slope of 0.02 ± 0.08 , consistent with no redshift evolution. We obtain correlation coefficients of $r = 0.016$ (for a sample of 69 data points) and $\rho = 0.06$, indicating a very low correlation probability of 0.41 (0.5σ).

It has been shown that DLAs show a significant evolution of their metallicity with redshift (Wolfe et al. 2005), with lower metallicities for high redshifts. For lower metallicities, one would expect to see, on average, weaker absorption features due to metal lines. For GRBs, this evolution is shallower (Fynbo et al. 2006; Thöne et al. 2012), so that it only becomes significant at very high-redshift. In our sample there are only 2 GRBs at $z > 5$ and, in those cases, we only have limits for their $LS P$. Although this could be indicative of a lower $LS P$, the sample is not big enough for a high- z study.

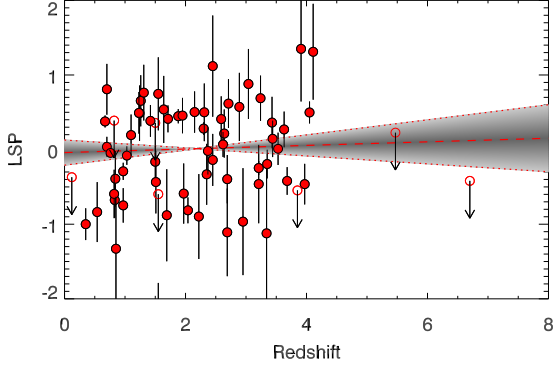


Fig. 17. Relation of the $LS P$ with redshift. The shaded region indicates the uncertainty in the slope of the linear fit.

4.2.6. Ionisation vs. E_{iso}

Here we compare the ionisation of the GRB environment, characterised by the difference between the high-ionisation $LS P$ ($LS P_H$) with the low-ionisation $LS P$ ($LS P_L$), with the isotropic equivalent energy release in γ -rays of the GRB (Butler et al. 2007; Sakamoto et al. 2011). Fig. 18 shows that the ionisation grows with E_{iso} , with correlation coefficients of $r = 0.35$ (for a sample of 35 data points) and $\rho = 0.30$, indicating a correlation probability of 0.92 (1.7σ). A linear fit gives $(LS P_H - LS P_L) = (0.41 \pm 0.19) \log(E_{iso}/erg) - (21.98 \pm 10.17)$.

Although this correlation is weak, it gives a hint of an interesting effect: It could mean that part of the ionisation that we see in afterglow spectra are due to the GRB, or that highly ionised hosts (probably due to intense star formation) produce more energetic GRBs. Part of the dispersion of this correlation can be caused by using the isotropic equivalent energy (where we assume that the energy is emitted isotropically) instead of the beaming-corrected energy (which is the real energy that is released through jets). Unfortunately, we do not have enough data to perform a study with the beaming-corrected energy.

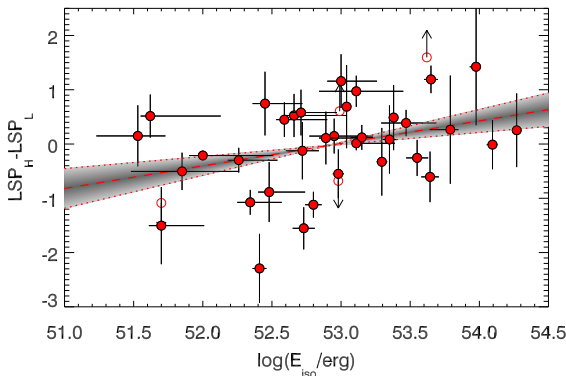


Fig. 18. Relation of the ionisation, characterised by $LS P_H - LS P_L$ with E_{iso} . The shaded region indicates the uncertainty in the slope of the linear fit.

4.2.7. $LS P$ vs. host galaxy absolute magnitude

In this section we compare the $LS P$ with the absolute host magnitude at a rest-frame wavelength of 1700 \AA . These data are obtained from Schulze et al. (in prep.), using the observations from the *TOUGH sample*¹ (Hjorth et al. 2012, Malesani in prep.), the *GHostS sample*² and the *Keck GRB host project imaging catalog*³. Figure 19 shows the fit of the $LS P$ versus host absolute magnitude comparison. In spite of the dispersion, there is a clear correlation that follows $LS P = (-0.27 \pm 0.08)M_{host,1700} - (5.02 \pm 1.59)$. We obtain correlation coefficients of $r = -0.62$ (for a sample of 19 data points) and $\rho = -0.64$, indicating a probability of correlation of 0.997 (2.7σ).

Larger, more luminous host galaxies, contain more material, and should produce, on average, stronger lines in the spectra of GRBs that they host. Due to the random location of the GRB within the galaxy, the relation between the strength of the lines and the host magnitude will have an intrinsic dispersion, which is also seen in the plot. We have done a similar exercise for $LS P_L$ and $LS P_H$ looking for differences in the correlation, which could be indicative of different locations for lower and higher ionised species within the host, such as a higher ionisation near the GRB, but found no significant difference.

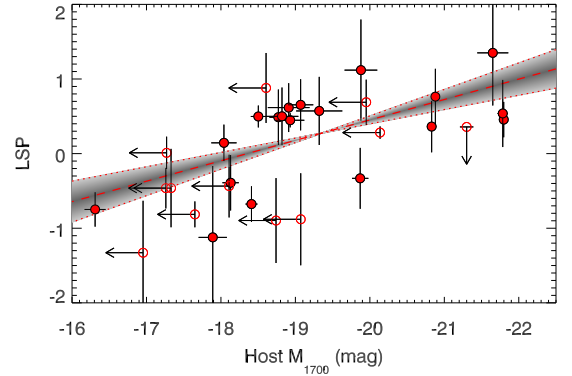


Fig. 19. Relation of the $LS P$ with host galaxy magnitude. The shaded region indicates the uncertainty in the slope of the linear fit.

4.2.8. $LS P$ vs. galaxy offset

In this final section we compare the $LS P$ with the projected offset of the GRB afterglow with respect to the centroid of the host galaxy. The offset values have been obtained from Malesani et al. (2012 in prep.). Figure 20 shows, in its lower panel, the $LS P$ versus the offset, using a colour coding for each object, where redder dots imply higher extinction and bluer ones lower extinction. Those objects for which there is no reliable extinction measurement are coloured black. The top panel shows the histogram of offsets, where we can see that the median offset is 1.16 kpc, similar to the value of 1.3 kpc obtained by Bloom et al. (2002) for an HST sample.

If the GRBs could happen at any position within the host galaxy, we would expect that the maximum $LS P$ would decline

¹ <http://www.dark-cosmology.dk/TOUGH>

² <http://www.grbhosts.org/>

³ <http://www.astro.caltech.edu/~dperley/hosts>

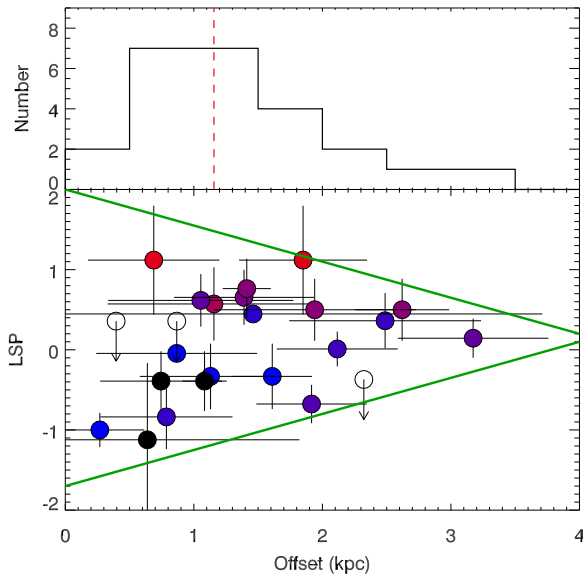


Fig. 20. Bottom: Relation of the LSP with the projected offset between the afterglow and the host galaxy. The colour coding indicates the extinction of the afterglow, being red the most extinguished and blue the least ones, those bursts without a reliable extinction measurement are indicated in black. Green lines are qualitative indicators of the distribution limits. Top: Histogram of offsets. The red-dashed line indicates the median offset.

as the offset increases, whereas the minimum LSP would be limited by the detectability of lines and would not depend on the offset. In Fig. 20 we see that the first statement is matched, but the second is not. We see how the minimum value of the LSP increases as we increase the offset. A possible explanation to this, is that GRBs only occur within limited areas of the host galaxies (e.g. the most prolific star forming regions). In this case there would be additional material, producing the minimum LSP in an extended region of the galaxy where no GRBs would form. Due to a projection effect, the minimum LSP value produced by this extended region of the host is higher for larger offsets, as depicted in Fig. 21 for a very simplified example. Figure 20 also shows how the bursts at the top of the distribution, which are the ones located behind most of the host galaxy material are also the ones that show the highest extinction, as one would expect. We have also considered if other biases would produce the increase in the minimum LSP with the offset, like having fainter afterglows at higher offsets, differences in the host galaxies, etc. Although we have not found evidence of any significant bias, we cannot discard other effects.

5. Summary and conclusions

We have used 69 low-resolution optical spectra of GRB afterglows, covering the redshift range $0.12 < z < 6.7$, to perform a statistical study of the rest-frame equivalent widths of strong absorption features. 61 of those spectra come from the sample presented by Fynbo et al. (2009) while the measurements of the other 8 are presented in this paper. The study includes 22 spectral features produced by 12 different atomic species. To obtain a consistent statistical analysis we include in our sample both detections and detection limits of these spectral features. A summary of the observations is presented in Tables 1 and 2. This collection of observations is used for the following:

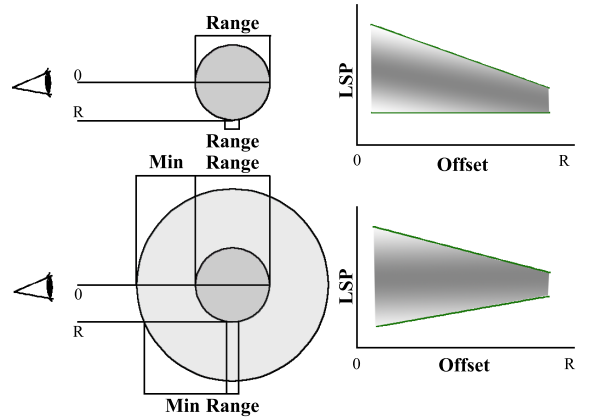


Fig. 21. Cartoon showing a limited region of the host in which the GRBs are generated (dark circle) and the effect that an extended region surrounding the previous (or the lack of it) would have in the distribution of LSP s as a function of the galaxy offsets. We indicate how the 'range' of intervening material from the inner region is reduced as the offset increases, while the the 'minimum' material, given by the extended region increases with the offset.

- For each spectral feature we calculate the average EW and its standard deviation, from which we obtain a picture of the typical GRB afterglow spectrum and the range of variations that can be expected.
- Using these values we propose the use of the EW diagrams as graphical tools to compare an individual GRB to the sample and give a catalogue with all our 69 spectra.
- As compared with a sample of quasar intervening DLA spectra, we find the GRB absorbers to be, on average, 2.5 times stronger and slightly more ionised. The difference of line strength is more significant in the case of the $C\text{IV}$ that is 3.4 times stronger in GRBs. There is also an excess in the $C\text{IV}\lambda 1549/\text{SiIV}\lambda 1403$ ratio. This excess of $C\text{IV}$ can be related to the existence of an excess of Wolf-Rayet stars in the environment of GRBs, consistent with the massive star origin of the explosions.
- We introduce the LSP as an overall measurement of the strength of the absorption features in a GRB spectrum relative to the sample as a single number. We give the distribution of LSP s so that one can derive, for a specific spectrum the percentile of line strength in which it lies. Similar LSP s are obtained for each GRB afterglow spectrum considering only low- and highly-ionised species respectively.
- We find correlations between the LSP and the extinction of the GRB, the hydrogen column density and the brightness of the host. However, the LSP is independent of the redshift and the time at which the observation was performed.
- There is a correlation between the ionisation of the absorbers in the GRB afterglow spectrum and the energy of the γ -ray emission, indicating that, either the GRB event is responsible for part of the ionisation, or galaxies with higher ionisation (i.e. stronger star formation) produce more energetic GRBs.
- When comparing the LSP with the projected offset between the host and the afterglow, we detect a decay in the maximum value as the afterglow lies further away from the galaxy, as it would be expected. However, we also detect an increase in the minimum LSP , which could be due to an observational bias that we did not consider, but also due to a geometric

effect that could provide information on the structure of the host galaxy. Larger samples will be needed to confirm this.

- Using the distributions of EWs of single species features we use a CoG fitting method to derive the distribution of their column densities and the number of components that make those features. For this we assume that the distribution of velocities of the absorbing atoms is described by $\langle \log(b/\text{km s}^{-1}) \rangle = 1.1$ and $\sigma_{\log(b/\text{km s}^{-1})} = 0.3$, as derived from line profile fitting of a sample of high resolution GRB spectra. From the fit we obtain that the average number of components that produce features in GRB afterglow spectra is $6.00^{+1.00}_{-1.25}$. The column densities of each of the species are given in Table 7.
- The most extreme ionisation ratios in our sample are found for GRBs with low neutral hydrogen column density. Whether this is due to ionisation by the GRB emission will have to be determined in further detailed studies.

Acknowledgements. We thank the anonymous referee for providing constructive comments. We thank Alexander Kann for fruitful discussions. The Dark Cosmology Centre is funded by the DNRF. This research has made use of the GHostS database (www.grbhosts.org), which is partly funded by Spitzer/NASA grant RSA Agreement No. 1287913. The research activity of AdUP, CT, RSR and JG is supported by Spanish research projects AYA2011-24780/ESP, AYA2009-14000-C03-01/ESP and AYA2010-21887-C04-01. JPUF and BMJ acknowledge support from the ERC-StG grant EGGs-278202. SS acknowledges support by a Grant of Excellence from the Icelandic Research Fund. GL is supported by the Swedish Research Council through grant No. 623-2011-7117. TZ is funded within the BINGO! (history of Baryons: INtergalactic medium/Galaxies cO-evolution) project by the Agence Nationale de la Recherche (ANR) under the allocation ANR-08-BLAN-0316-01.

References

- Berger, E., Fox, D. B., Cucchiara, A., & Cenko, S. B. 2008, GRB Coordinates Network, 8335
- Berger, E., Penprase, B. E., Cenko, S. B., et al. 2006, ApJ, 642, 979
- Bloom, J. S., Kulkarni, S. R., & Djorgovski, S. G. 2002, AJ, 123, 1111
- Butler, N. R., Kocevski, D., Bloom, J. S., & Curtis, J. L. 2007, ApJ, 671, 656
- Campana, S., Thöne, C. C., de Ugarte Postigo, A., et al. 2010, MNRAS, 402, 2429
- Christensen, L., Fynbo, J. P. U., Prochaska, J. X., et al. 2011, ApJ, 727, 73
- Christensen, L., Hjorth, J., & Gorosabel, J. 2004, A&A, 425, 913
- Cucchiara, A., Levan, A. J., Fox, D. B., et al. 2011, ApJ, 736, 7
- D’Avanzo, P., D’Elia, V., & Covino, S. 2008, GRB Coordinates Network, 8345
- de Ugarte Postigo, A., Gorosabel, J., Fynbo, J. P. U., Wiersema, K., & Tanvir, N. 2009a, GRB Coordinates Network, 9771
- de Ugarte Postigo, A., Gorosabel, J., Malesani, D., Fynbo, J. P. U., & Levan, A. J. 2009b, GRB Coordinates Network, 9381
- de Ugarte Postigo, A., Gorosabel, J., Malesani, D., Fynbo, J. P. U., & Levan, A. J. 2009c, GRB Coordinates Network, 9383
- de Ugarte Postigo, A., Jakobsson, P., Malesani, D., et al. 2009d, GRB Coordinates Network, 8766
- D’Elia, V., Campana, S., Covino, S., et al. 2011, MNRAS, 418, 680
- D’Elia, V., Fiore, F., Meurs, E. J. A., et al. 2007, A&A, 467, 629
- D’Elia, V., Fiore, F., Perna, R., et al. 2009, ApJ, 694, 332
- Fox, A. J., Ledoux, C., Vreeswijk, P. M., Smette, A., & Jaunsen, A. O. 2008, A&A, 491, 189
- Fruchter, A. S., Levan, A. J., Strolger, L., et al. 2006, Nature, 441, 463
- Fynbo, J. P. U., Jakobsson, P., Prochaska, J. X., et al. 2009, ApJS, 185, 526
- Fynbo, J. P. U., Prochaska, J. X., Sommer-Larsen, J., Dessauges-Zavadsky, M., & Møller, P. 2008, ApJ, 683, 321
- Fynbo, J. P. U., Starling, R. L. C., Ledoux, C., et al. 2006, A&A, 451, L47
- Galama, T. J., Vreeswijk, P. M., van Paradijs, J., et al. 1998, Nature, 395, 670
- Hjorth, J., Malesani, D., Jakobsson, P., et al. 2012, ApJ, 756, 187
- Jakobsson, P., de Ugarte Postigo, A., Gorosabel, J., et al. 2009, GRB Coordinates Network, 9797
- Jakobsson, P., Fynbo, J. P. U., Ledoux, C., et al. 2006a, A&A, 460, L13
- Jakobsson, P., Levan, A., Fynbo, J. P. U., et al. 2006b, A&A, 447, 897
- Kann, D. A., Klose, S., Zhang, B., et al. 2010, ApJ, 720, 1513
- Kann, D. A., Masetti, N., & Klose, S. 2007, AJ, 133, 1187
- Lazzati, D., Perna, R., & Ghisellini, G. 2001, MNRAS, 325, L19
- Malesani, D., Fynbo, J. P. U., D’Elia, V., et al. 2009, GRB Coordinates Network, 9457

- Morton, D. C. 2003, ApJS, 149, 205
- Noterdaeme, P., Petitjean, P., Ledoux, C., & Srianand, R. 2009, A&A, 505, 1087
- Piranomonte, S., Ward, P. A., Fiore, F., et al. 2008, A&A, 492, 775
- Pontzen, A., Deason, A., Governato, F., et al. 2010, MNRAS, 402, 1523
- Prochaska, J. X., Chen, H.-W., Dessauges-Zavadsky, M., & Bloom, J. S. 2007, ApJ, 666, 267
- Prochter, G. E., Prochaska, J. X., Chen, H.-W., et al. 2006, ApJ, 648, L93
- Racusin, J. L., Karpov, S. V., Sokolowski, M., et al. 2008, Nature, 455, 183
- Sakamoto, T., Barthelmy, S. D., Baumgartner, W. H., et al. 2011, ApJS, 195, 2
- Salvaterra, R., Della Valle, M., Campana, S., et al. 2009, Nature, 461, 1258
- Savaglio, S., Fall, S. M., & Fiore, F. 2003, ApJ, 585, 638
- Schady, P., Page, M. J., Oates, S. R., et al. 2010, MNRAS, 401, 2773
- Svensson, K. M., Levan, A. J., Tanvir, N. R., Fruchter, A. S., & Strolger, L.-G. 2010, MNRAS, 405, 57
- Tanvir, N. R., Fox, D. B., Levan, A. J., et al. 2009, Nature, 461, 1254
- Tejos, N., Lopez, S., Prochaska, J. X., Chen, H.-W., & Dessauges-Zavadsky, M. 2007, ApJ, 671, 622
- Thöne, C. C., Campana, S., Lazzati, D., et al. 2011, MNRAS, 414, 479
- Thöne, C. C., Fynbo, J. P. U., Goldoni, P., et al. 2012, arXiv:1206.2337
- Thöne, C. C., Jakobsson, P., De Cia, A., et al. 2009, GRB Coordinates Network, 9409
- Vergani, S. D., Petitjean, P., Ledoux, C., et al. 2009, A&A, 503, 771
- Vreeswijk, P. M., Ledoux, C., Smette, A., et al. 2007, A&A, 468, 83
- Watson, D., Hjorth, J., Fynbo, J. P. U., et al. 2007, ApJ, 660, L101
- Watson, D., & Jakobsson, P. 2012, ApJ, 754, 89
- Wolfe, A. M., Gawiser, E., & Prochaska, J. X. 2005, ARA&A, 43, 861
- Zafar, T., Watson, D., Fynbo, J. P. U., et al. 2011, A&A, 532, A143

Table 1. Rest-frame EWs (in Å) of lines with wavelength below 2000Å. The table displays detections or upper limits ($3\text{-}\sigma$) whenever the spectrum covers the range of the feature and the feature is not affected by strong telluric absorptions.

GRB	z	1260 Si II	1303 O I/Si II/O I*	1335 C II/C II*	1394 Si IV	1403 Si IV	1527 Si II	1549 C IV/C IV	1608 Fe II	1671 Al II	1855 Al III	1863 Al III
050319	3.24	1.82± 0.55	2.70± 0.75	2.17± 0.55	< 2.05	2.15± 0.67	< 2.27	< 2.26	< 2.57	—	—	—
050401	2.89	< 3.39	3.60± 1.03	3.08± 0.77	< 3.60	< 1.53	3.08± 0.51	2.57± 0.26	2.19± 0.39	1.80± 0.36	1.93± 0.18	1.93 ± 0.21
050408	1.24	—	—	—	—	—	—	—	—	—	—	—
050730	3.97	1.11± 0.06	< 1.43	0.99± 0.04	0.82± 0.03	0.46± 0.05	—	—	0.26± 0.04	0.62± 0.06	—	—
050802	1.71	—	< 14.18	< 4.66	< 2.48	< 2.04	< 1.58	2.73± 0.55	< 1.63	< 1.44	< 1.08	< 0.97
050824	0.83	—	—	—	—	—	—	—	—	—	—	—
050908	3.34	< 0.08	0.30± 0.05	0.14± 0.04	< 1.50	0.59± 0.04	< 0.61	3.23± 0.05	—	< 0.15	< 0.18	< 0.18
050922C	2.22	0.65± 0.06	< 2.17	0.31± 0.06	0.47± 0.03	0.43± 0.03	0.62± 0.03	1.27± 0.03	0.19± 0.03	0.84± 0.03	< 0.10	< 0.11
060115	3.53	< 1.19	2.54± 0.40	1.90± 0.40	< 1.02	< 1.04	1.39± 0.35	1.32± 0.35	< 1.29	—	< 2.63	< 2.29
060124	2.30	< 0.85	< 0.64	< 0.70	1.09± 0.28	< 0.50	< 0.39	2.93± 0.22	< 0.32	< 0.35	< 0.33	< 0.33
060206	4.05	< 2.37	2.78± 0.02	2.27± 0.03	—	—	—	—	—	—	—	—
060210	3.91	4.42± 0.09	4.85± 0.08	4.32± 0.08	3.05± 0.06	1.98± 0.03	3.67± 0.04	8.63± 0.05	1.61± 0.04	—	—	—
060502A	1.50	—	—	—	—	—	—	—	—	—	< 2.95	< 2.78
060526	3.21	1.43± 0.07	1.78± 0.10	1.78± 0.10	< 0.18	< 0.16	0.78± 0.10	0.45± 0.10	< 0.15	0.86± 0.10	—	< 0.33
060614	0.12	—	—	—	—	—	—	—	—	—	—	—
060707	3.43	< 1.00	3.43± 0.70	2.35± 0.29	< 0.53	< 0.53	2.30± 0.32	1.29± 0.27	< 0.58	2.12± 0.36	< 0.78	< 0.79
060714	2.71	1.94± 0.16	3.42± 0.16	2.83± 0.13	1.56± 0.11	1.35± 0.11	1.83± 0.13	3.53± 0.11	1.35± 0.13	2.05± 0.13	2.45± 0.13	1.16 ± 0.13
060729	0.54	—	—	—	—	—	—	—	—	—	—	—
060904B	0.70	—	—	—	—	—	—	—	—	—	—	—
060906	3.68	0.85± 0.21	1.18± 0.24	1.30± 0.19	0.68± 0.17	< 0.34	< 0.42	< 0.47	< 0.47	—	< 0.76	< 0.67
060908	1.88	—	—	—	< 1.33	< 1.40	< 0.89	3.23± 0.52	< 0.71	< 1.08	< 0.43	< 0.43
060926	3.21	< 0.74	< 0.72	1.31± 0.33	< 0.73	< 0.73	0.95± 0.26	1.90± 0.29	< 0.41	—	—	—
060927	5.47	< 1.29	< 2.96	< 2.67	—	—	—	—	—	—	—	—
061007	1.26	—	—	—	—	—	—	—	< 8.18	< 6.73	< 3.70	< 3.62
061021	0.35	—	—	—	—	—	—	—	—	—	—	—
061110A	0.76	—	—	—	—	—	—	—	—	—	< 12.17	< 11.69
061110B	3.44	< 2.28	2.61± 0.47	1.51± 0.32	1.49± 0.27	1.33± 0.29	0.72± 0.18	—	< 0.44	0.92± 0.29	< 0.76	< 0.80
061121	1.31	—	—	—	—	—	2.05± 0.06	4.42± 0.06	1.93± 0.03	2.35± 0.03	2.03± 0.03	1.62 ± 0.03
070110	2.35	1.34± 0.12	2.12± 0.12	1.13± 0.09	0.42± 0.09	0.42± 0.09	1.04± 0.09	0.93± 0.09	0.75± 0.09	0.90± 0.09	0.33± 0.09	0.30 ± 0.09
070125	1.55	—	—	—	—	—	< 0.25	0.67± 0.12	< 0.19	< 0.16	< 0.14	< 0.14
070306	1.50	—	—	—	—	—	< 9.25	< 7.64	< 5.84	< 4.21	< 3.37	< 3.31
070318	0.84	—	—	—	—	—	—	—	—	—	—	—
070411	2.95	0.28± 0.08	0.33± 0.08	0.71± 0.13	0.78± 0.10	0.66± 0.10	0.43± 0.10	2.56± 0.13	< 0.13	0.46± 0.08	—	—
070419A	0.97	—	—	—	—	—	—	—	—	—	—	—
070506	2.31	2.72± 0.30	3.23± 0.33	< 1.31	1.42± 0.21	2.15± 0.27	1.75± 0.12	2.99± 0.15	1.42± 0.09	1.24± 0.09	1.12± 0.06	0.51 ± 0.06
070508	0.82	—	—	—	—	—	—	—	—	—	—	—
070611	2.04	< 0.92	< 0.92	< 0.94	< 0.78	< 0.77	< 0.67	< 0.65	< 0.59	< 0.52	< 0.41	< 0.40
070721B	3.63	< 1.30	1.40± 0.41	< 0.89	1.30± 0.41	1.51± 0.48	1.25± 0.41	3.15± 0.56	< 1.02	—	< 1.33	< 1.91
070802	2.45	< 5.70	< 4.56	< 3.91	< 2.70	< 2.57	2.90± 0.58	2.12± 0.52	3.04± 0.46	4.14± 0.35	< 0.70	< 0.82
071020	2.15	< 5.33	< 4.87	< 4.08	< 3.19	< 3.42	< 2.36	< 2.16	< 1.84	1.90± 0.63	< 0.99	< 1.01
071031	2.69	0.72± 0.04	1.33± 0.03	1.21± 0.04	1.00± 0.04	0.75± 0.04	0.54± 0.03	2.18± 0.04	0.88± 0.04	0.63± 0.03	0.26± 0.03	—
071112C	0.82	—	—	—	—	—	—	—	—	—	—	—
080210	2.64	1.15± 0.19	2.66± 0.16	2.39± 0.14	1.57± 0.11	1.29± 0.11	1.40± 0.08	3.49± 0.11	1.02± 0.08	1.70± 0.08	1.07± 0.08	0.66 ± 0.08
080319B	0.97	—	—	—	—	—	—	—	—	—	< 3.44	< 3.23
080319C	1.95	—	—	< 2.88	< 1.98	< 1.87	< 0.95	3.59± 0.24	< 0.67	1.93± 0.31	1.46± 0.20	1.42 ± 0.20
080330	1.51	—	—	—	—	—	< 0.92	1.71± 0.28	< 0.74	< 0.62	< 0.44	< 0.44

Table 1. continued.

GRB	z	1260 Si II	1303 O I/Si II/O I*	1335 C II/C II*	1394 Si IV	1403 Si IV	1527 Si II	1549 C IV/C IV	1608 Fe II	1671 Al II	1855 Al III	1863 Al III
080411	1.03	—	—	—	—	—	—	—	—	—	—	0.70 ± 0.05
080413B	1.10	—	—	—	—	—	—	—	< 0.09	2.33 ± 0.48	0.38 ± 0.10	0.38 ± 0.10
080520	1.55	—	—	—	—	—	< 8.69	< 10.25	< 4.74	< 6.59	< 4.40	< 4.35
080603B	2.69	< 0.11	0.72 ± 0.04	1.05 ± 0.04	0.51 ± 0.04	0.34 ± 0.04	0.15 ± 0.04	1.19 ± 0.04	< 0.33	0.42 ± 0.04	—	—
080604	1.42	—	—	—	—	—	—	—	—	—	—	—
080605	1.64	—	—	< 6.89	< 3.89	< 2.74	1.97 ± 0.23	5.11 ± 0.30	0.61 ± 0.19	2.31 ± 0.19	2.12 ± 0.11	1.55 ± 0.11
080607	3.04	—	—	—	2.67 ± 0.10	1.45 ± 0.07	1.94 ± 0.04	5.15 ± 0.06	3.67 ± 0.05	2.29 ± 0.02	1.84 ± 0.03	1.52 ± 0.04
080707	1.23	—	—	—	—	—	—	—	—	—	< 1.28	< 1.26
080710	0.85	—	—	—	—	—	—	—	—	—	—	—
080721	2.59	1.75 ± 0.19	1.70 ± 0.19	1.98 ± 0.19	1.34 ± 0.14	0.84 ± 0.14	1.67 ± 0.11	4.46 ± 0.17	2.45 ± 0.14	1.42 ± 0.11	< 0.23	< 0.24
080810	3.35	< 0.42	< 0.43	< 0.43	< 0.39	< 0.41	0.48 ± 0.14	3.13 ± 0.21	—	—	—	—
080905B	2.37	< 1.86	2.67 ± 0.59	< 1.18	< 0.87	< 0.84	0.74 ± 0.24	1.66 ± 0.21	< 0.43	1.01 ± 0.18	0.80 ± 0.18	< 0.41
080913	6.70	< 0.78	< 1.51	< 7.87	—	—	—	—	—	—	—	—
080916A	0.67	—	—	—	—	—	—	—	—	—	—	—
080928	1.69	—	< 2.14	< 1.44	< 1.01	< 0.90	< 0.49	2.12 ± 0.26	0.52 ± 0.15	< 0.32	< 0.26	< 0.26
081007	0.53	—	—	—	—	—	—	—	—	—	—	—
081008	1.97	1.04 ± 0.24	1.58 ± 0.17	1.41 ± 0.10	0.47 ± 0.07	0.44 ± 0.07	0.63 ± 0.05	1.04 ± 0.07	0.59 ± 0.05	0.79 ± 0.04	0.29 ± 0.04	0.17 ± 0.04
090102	1.55	—	—	—	—	—	< 2.19	3.50 ± 0.65	3.05 ± 0.48	1.86 ± 0.39	1.58 ± 0.29	0.67 ± 0.20
090516	4.11	< 6.83	< 6.83	5.81 ± 0.04	2.84 ± 0.04	1.72 ± 0.04	4.05 ± 0.06	5.87 ± 0.10	3.09 ± 0.06	4.54 ± 0.06	< 4.04	< 2.39
090519	3.85	< 1.59	< 2.24	< 1.95	< 1.45	< 1.59	< 2.78	< 1.63	—	< 2.55	< 6.22	< 3.72
090529	2.62	< 2.04	< 1.64	< 1.52	< 1.50	< 1.34	1.93 ± 0.44	1.71 ± 0.47	< 1.43	< 1.25	< 1.18	< 1.17
090812	2.45	1.11 ± 0.24	2.20 ± 0.30	1.94 ± 0.21	0.54 ± 0.13	0.57 ± 0.12	0.76 ± 0.13	1.12 ± 0.13	1.87 ± 0.17	1.12 ± 0.08	0.57 ± 0.08	0.75 ± 0.14
090814A	0.70	—	—	—	—	—	—	—	—	—	—	—

Table 2. Rest-frame EWs of lines with wavelength above 2000Å. The table displays detections or upper limits ($3\text{-}\sigma$) whenever the spectrum covers the range of the feature and the feature is not affected by strong telluric absorptions.

GRB	z	2026 Zn II/Cr II	2062 Cr II/Zn II	2344 Fe II/Fe II*	2374 Fe II	2383 Fe II/Fe II*	2587 Fe II	2600 Fe II*/Fe II	2800 Mg II	2852 Mg I	3935 Ca II	3970 Ca II
050319	3.24	—	—	—	—	—	—	—	—	—	—	—
050401	2.89	1.47 ± 0.21	1.44 ± 0.23	1.41 ± 0.18	1.59 ± 0.26	1.59 ± 0.26	—	—	—	—	—	—
050408	1.24	< 1.58	2.75 ± 0.67	2.45 ± 0.34	1.34 ± 0.30	1.88 ± 0.29	1.58 ± 0.19	3.50 ± 0.25	4.87 ± 0.29	1.55 ± 0.17	< 0.35	—
050730	3.97	—	—	—	—	—	—	—	—	—	—	—
050802	1.71	< 0.90	< 1.59	2.62 ± 0.33	< 0.87	2.69 ± 0.33	1.85 ± 0.41	—	—	—	—	—
050824	0.83	< 4.84	< 2.36	0.98 ± 0.27	< 2.46	< 2.46	0.82 ± 0.22	< 0.57	2.19 ± 0.33	< 0.49	< 0.49	< 0.41
050908	3.34	1.15 ± 0.23	—	—	—	—	—	—	—	—	—	—
050922C	2.22	< 0.14	< 0.13	—	—	—	—	—	—	—	—	—
060115	3.53	—	—	—	—	—	—	—	—	—	—	—
060124	2.30	< 0.23	< 0.34	—	—	< 0.80	—	—	—	—	—	—
060206	4.05	—	—	—	—	—	—	—	—	—	—	—
060210	3.91	—	—	—	—	—	—	—	—	—	—	—
060502A	1.50	< 0.71	< 0.59	0.92 ± 0.22	1.09 ± 0.12	2.40 ± 0.11	0.83 ± 0.10	1.56 ± 0.09	3.60 ± 0.11	0.90 ± 0.08	< 0.17	—
060526	3.21	< 0.36	< 0.36	—	—	—	—	—	—	—	—	—
060614	0.12	—	—	—	—	—	—	—	—	—	—	< 0.99
060707	3.43	—	—	—	—	—	—	—	—	—	—	—
060714	2.71	< 0.16	—	2.16 ± 0.30	1.83 ± 0.27	2.59 ± 0.27	—	—	—	—	—	—
060729	0.54	—	—	< 0.37	< 0.29	< 0.25	< 0.05	0.45 ± 0.13	1.82 ± 0.04	0.59 ± 0.04	0.75 ± 0.03	0.55 ± 0.03
060904B	0.70	—	—	—	—	—	0.94 ± 0.18	1.82 ± 0.18	4.65 ± 0.12	1.00 ± 0.12	1.35 ± 0.12	1.06 ± 0.12
060906	3.68	—	—	—	—	—	—	—	—	—	—	—
060908	1.88	< 0.36	< 0.34	—	—	—	—	—	—	—	—	—
060926	3.21	< 0.76	< 1.05	—	—	—	—	—	—	—	—	—
060927	5.47	—	—	—	—	—	—	—	—	—	—	—
061007	1.26	< 2.84	< 2.64	2.83 ± 0.75	3.54 ± 0.88	2.26 ± 0.66	3.23 ± 0.58	2.61 ± 0.62	5.40 ± 0.97	< 1.10	< 1.04	—
061021	0.35	—	—	—	—	—	—	—	1.85 ± 0.52	< 0.96	< 0.82	< 0.49
061110A	0.76	< 6.60	< 6.27	< 3.41	< 3.36	< 3.46	< 2.85	< 2.81	3.64 ± 0.80	< 2.23	< 2.32	—
061110B	3.44	—	—	—	—	—	—	—	—	—	—	—
061121	1.31	1.05 ± 0.03	1.00 ± 0.03	2.83 ± 0.03	2.60 ± 0.03	3.69 ± 0.03	3.18 ± 0.04	3.81 ± 0.03	8.64 ± 0.05	2.47 ± 0.04	1.76 ± 0.08	1.43 ± 0.07
070110	2.35	0.60 ± 0.12	—	0.87 ± 0.24	0.99 ± 0.18	2.12 ± 0.24	< 0.82	2.03 ± 0.18	< 1.76	< 1.24	—	—
070125	1.55	< 0.13	< 0.13	< 0.13	< 0.13	< 0.13	< 0.13	< 0.13	0.35 ± 0.08	< 0.14	< 0.19	—
070306	1.50	< 2.71	< 2.65	< 2.70	< 2.68	< 2.60	< 2.50	< 2.52	—	—	< 2.35	—
070318	0.84	< 0.91	< 0.70	0.76 ± 0.16	0.43 ± 0.11	1.20 ± 0.16	< 3.64	< 3.64	2.61 ± 0.16	0.65 ± 0.11	2.07 ± 0.22	0.98 ± 0.22
070411	2.95	—	—	—	—	—	—	—	—	—	—	—
070419A	0.97	—	—	—	—	—	—	—	—	—	1.25 ± 0.16	0.61 ± 0.15
070506	2.31	0.94 ± 0.21	0.88 ± 0.24	—	—	—	—	—	—	—	—	—
070508	0.82	—	—	< 8.79	< 8.21	< 7.80	< 5.72	< 5.72	< 4.96	< 4.95	< 4.83	< 3.56
070611	2.04	< 0.40	< 0.42	< 0.53	< 0.55	< 0.61	< 0.82	< 0.68	2.11 ± 0.69	< 0.65	< 0.87	—
070721B	3.63	< 8.24	—	—	—	—	—	—	—	—	—	—
070802	2.45	1.22 ± 0.29	< 0.86	4.78 ± 0.58	3.68 ± 0.43	5.45 ± 0.43	5.65 ± 0.38	8.41 ± 0.38	—	—	—	—
071020	2.15	< 1.06	< 1.10	< 1.38	< 1.44	1.90 ± 0.63	2.22 ± 0.63	3.49 ± 0.63	7.62 ± 0.13	< 2.36	< 1.57	—
071031	2.69	< 0.10	—	1.17 ± 0.07	0.66 ± 0.09	1.21 ± 0.05	0.93 ± 0.16	1.40 ± 0.09	—	—	—	—
071112C	0.82	< 2.77	< 1.99	1.10 ± 0.27	< 0.71	0.88 ± 0.27	1.10 ± 0.27	1.32 ± 0.27	2.69 ± 0.33	< 0.58	< 0.51	< 0.73
080210	2.64	0.63 ± 0.11	< 0.16	1.73 ± 0.11	0.49 ± 0.14	1.87 ± 0.14	< 0.54	< 0.77	—	—	—	—
080319B	0.97	< 0.90	< 0.94	< 0.67	< 0.64	< 0.62	0.91 ± 0.25	< 0.53	1.88 ± 0.51	< 0.50	< 0.49	—
080319C	1.95	0.78 ± 0.24	0.78 ± 0.20	—	—	—	—	—	—	—	—	—
080330	1.51	1.71 ± 0.16	< 0.37	< 0.53	< 0.36	0.88 ± 0.20	< 0.36	< 0.36	2.07 ± 0.12	—	< 0.39	—

Table 2. continued.

GRB	z	2026 Zn II/Cr II	2062 Cr II/Zn II	2344 Fe II/Fe II*	2374 Fe II	2383 Fe II/Fe II*	2587 Fe II	2600 Fe II*/Fe II	2800 Mg II	2852 Mg I	3935 Ca II	3970 Ca II
080411	1.03	0.64 ± 0.03	0.55 ± 0.04	< 1.41	< 4.59	< 4.59	< 4.12	< 4.12	3.17 ± 0.07	0.58 ± 0.05	1.08 ± 0.15	1.11 ± 0.15
080413B	1.10	0.67 ± 0.10	0.67 ± 0.05	2.17 ± 0.04	1.45 ± 0.07	2.42 ± 0.07	< 7.54	< 7.54	6.38 ± 0.10	1.04 ± 0.05	—	—
080520	1.55	< 3.36	< 3.46	< 3.21	< 3.15	< 3.09	< 2.65	< 2.62	< 2.45	< 2.46	< 2.61	—
080603B	2.69	—	—	—	—	—	—	—	—	—	—	—
080604	1.42	—	—	1.98 ± 0.29	1.78 ± 0.25	1.94 ± 0.25	2.64 ± 0.21	2.64 ± 0.21	5.37 ± 0.37	< 0.37	—	—
080605	1.64	0.61 ± 0.11	0.38 ± 0.11	2.50 ± 0.11	< 4.39	< 4.39	2.12 ± 0.11	—	8.56 ± 0.23	2.31 ± 0.11	< 0.25	—
080607	3.04	1.57 ± 0.04	—	—	—	—	—	—	—	—	—	—
080707	1.23	< 1.25	< 1.16	2.29 ± 0.40	< 0.79	2.38 ± 0.40	1.75 ± 0.36	2.06 ± 0.36	7.35 ± 0.49	2.20 ± 0.36	< 0.85	< 3.28
080710	0.85	—	—	0.42 ± 0.03	0.21 ± 0.02	0.57 ± 0.02	0.41 ± 0.02	0.71 ± 0.02	2.26 ± 0.02	0.36 ± 0.02	< 0.03	—
080721	2.59	< 0.33	< 0.31	—	—	—	—	—	—	—	—	—
080810	3.35	—	—	—	—	—	—	—	—	—	—	—
080905B	2.37	0.59 ± 0.18	0.83 ± 0.15	1.51 ± 0.30	1.57 ± 0.18	1.28 ± 0.21	1.51 ± 0.18	1.66 ± 0.42	5.93 ± 1.19	< 1.55	< 1.08	—
080913	6.70	—	—	—	—	—	—	—	—	—	—	—
080916A	0.67	—	—	< 3.05	< 3.86	< 3.74	< 2.55	< 2.46	4.91 ± 0.84	< 2.12	< 1.80	< 1.51
080928	1.69	< 0.22	< 0.23	0.74 ± 0.15	0.63 ± 0.11	0.45 ± 0.07	0.52 ± 0.07	0.82 ± 0.11	2.38 ± 0.22	< 0.25	—	—
081007	0.53	—	—	—	—	—	—	—	—	—	—	> 18.80
081008	1.97	0.29 ± 0.05	0.24 ± 0.05	—	—	—	—	—	—	—	—	—
090102	1.55	< 0.95	< 0.94	2.97 ± 0.87	< 1.11	2.49 ± 0.78	2.46 ± 0.45	3.66 ± 0.51	10.13 ± 0.63	5.00 ± 0.93	< 1.93	—
090516	4.11	—	—	—	—	—	—	—	—	—	—	—
090519	3.85	—	—	—	—	—	—	—	—	—	—	—
090529	2.62	< 1.72	< 1.67	< 2.13	< 2.40	< 2.94	< 5.25	< 7.27	—	—	—	—
090812	2.45	0.55 ± 0.08	0.50 ± 0.07	1.04 ± 0.09	1.19 ± 0.10	1.81 ± 0.10	1.24 ± 0.21	1.61 ± 0.14	< 23.03	< 43.12	—	—
090814A	0.70	—	—	< 14.05	< 12.83	< 12.83	< 12.83	< 14.05	4.16 ± 0.79	< 12.83	2.51 ± 0.66	2.69 ± 0.72

Appendix A: Additional spectra

In this section we present further spectra complementing the sample of Fynbo et al. (2009), analysed in an equivalent way.

A.1. GRB 081007

This spectrum has not yet been published. It was a 2700s exposure obtained with FORS2 at the VLT using the 300I grating. It shows evidence of 2 emission lines (see Table A.1 and Fig. A.1) at a redshift of $z = 0.530$, in agreement of the redshift suggested by Berger et al. (2008). The lack of [O III] λ 5008 is probably due to contamination by a sky line.

Table A.1. GRB 081007 ($z = 0.530$). Observed-frame equivalent widths.

Wavelength	Feature	z	EW
7438.2	H- β 4862.68	0.5297	emission
7589.5	[OIII] 4960.29	0.5300	emission

A.2. GRB 081008

The data presented here (see Table A.2 and Fig. A.2) were initially published as a GCN circular (D'Avanzo et al. 2008) and later in a more detailed study (D'Elia et al. 2011). The observation was performed using FORS2 at the VLT with the 600B grating and consisted of 3×900 s exposure. We obtain a redshift of 1.969 ± 0.001 , consistent with the value determined by D'Elia et al. (2011). From the fit of the Ly α absorption, we determine a neutral hydrogen column density of $\log(N_{\text{H I}}/\text{cm}^{-2}) = 21.59 \pm 0.10$.

Table A.2. GRB 081008 ($z = 1.969$). Observed-frame equivalent widths.

Wavelength	Feature	z	EW
3741.5	SII+SiII 1259.9	1.9696	3.1 \pm 0.7
3755.7	SII* 1264.74	1.9695	1.5 \pm 0.4
3793.1	CI 1277.25	1.9697	3.1 \pm 0.7
3865.9	OI 1302.17	1.9689	4.7 \pm 0.5
3874.1	SiII 1304.37	1.9701	
3887.5	SiII*1309.28	1.9692	1.2 \pm 0.3
3964.3	CII 1334.53	1.9706	4.2 \pm 0.3
4138.5	SiIV 1393.76	1.9693	1.4 \pm 0.2
4165.4	SiIV 1402.77	1.9694	1.3 \pm 0.2
4434.0	?		1.7 \pm 0.3
4532.5	SiII 1526.71	1.9688	1.88 \pm 0.14
4553.0	SiII* 1533.43	1.9692	1.13 \pm 0.13
4600.	CIV+CIV 1549		3.1 \pm 0.2
4775.4	FeII 1608.45	1.9690	1.74 \pm 0.15
4786.2	FeII 1611.20	1.9706	0.90 \pm 0.19
4811.6	?		0.84 \pm 0.19
4960.5	AlII 1670.79	1.9690	2.34 \pm 0.13
5053.9	?		0.51 \pm 0.11
5367.9	SiII 1808.01	1.9690	0.76 \pm 0.12
5506.8	AlIII 1854.72	1.9691	0.87 \pm 0.12
5530.8	AlIII 1862.79	1.9691	0.51 \pm 0.13
6015.7	ZnII 2026.14	1.9690	0.85 \pm 0.15
6105.5	CrII 2056.26	1.9692	0.76 \pm 0.14
6123.2	CrII+ZnII 2062.4	1.9690	0.72 \pm 0.14
6133.9	CrII 2066.16	1.9687	0.43 \pm 0.15

A.3. GRB 090102

The spectrum presented here (see Table A.3 and Fig. A.3) has only been published in a GCN (de Ugarte Postigo et al. 2009d). The spectrum an exposure time of 2700s and was obtained with AIFOSC at the 2.5m NOT telescope. From the absorption features we determine a redshift of 1.548 ± 0.001 .

Table A.3. GRB 090102 ($z = 1.548$). Observed-frame equivalent widths.

Wavelength	Feature	z	EW
3949.6	CIV+CIV 1549		8.9 \pm 0.17
4096.0	FeII 1608.45	1.5466	7.8 \pm 1.2
4257.7	AlII 1670.79	1.5483	4.7 \pm 1.0
4728.8	AlIII 1854.72	1.5496	4.0 \pm 0.7
4746.4	AlIII 1862.79	1.5480	1.7 \pm 0.5
5975.1	FeII 2344.2	1.5489	7.6 \pm 2.2
6055.8	FeII 2374.5	1.5503	5.3 \pm 2.0
6072.4	FeII 2382.8	1.5484	6.4 \pm 2.0
6590.9	FeII 2587	1.5480	6.3 \pm 1.1
6620.4	FeII 2600	1.5461	9.3 \pm 1.3
7134.0	MgII+MgII 2800		25.8 \pm 1.6
7266.9	MgI 2852	1.5471	12.74 \pm 2.4

A.4. GRB 090516

The spectrum of GRB 090516 (see Table A.4 and Fig. A.4) has, until now, only been reported in GCNs (de Ugarte Postigo et al. 2009b,c). It was obtained with FORS2 at the VLT with the 300V grism and an exposure of 2×1800 s. From the absorption features we determine a redshift of 4.111 ± 0.006 . By fitting the Ly α absorption we determine a neutral hydrogen column density of $\log(N_{\text{H I}}/\text{cm}^{-2}) = 21.70 \pm 0.10$.

A.5. GRB 090519

This spectrum has been only reported in a GCN circular (Thöne et al. 2009). It was obtained with FORS2 at the VLT and grism 300V with an exposure time of 3×1800 s. The spectrum has low signal to noise ratio and shows no absorption features (see Fig. A.5) and the redshift is determined by the identification of the Lyman break as well as broad absorptions of Ly α and Ly β .

A.6. GRB 090529

These data have been only reported in a GCN (Malesani et al. 2009). The spectrum is a 2×1800 s exposure obtained using FORS2 with grism 300V at the VLT. From a limited amount of absorption features (see Table A.5 and Fig. A.6) we determine a redshift of 2.624 ± 0.003 .

A.7. GRB 090812

The data presented here (see Table A.6 and Fig. A.7) have previously been published only in the GCN circulars (de Ugarte Postigo et al. 2009a). It is a FORS2 spectrum from the VLT, which shows multiple absorption features at a common redshift of 2.4521 ± 0.0010 . From the Ly α absorption we determine a neutral hydrogen column density of $\log(N_{\text{H I}}/\text{cm}^{-2}) = 22.30 \pm 0.10$.

Table A.4. GRB 090516 ($z = 4.111 \pm 0.006$). Observed-frame equivalent widths.

Wavelength	Feature	z	EW
6327.8	NV 1232.8	4.1329	12.4 +/- 0.3
6347.9	NV 1242.9	4.1073	
6393.6	SII 1250.6	4.1124	35.6 + 0.3
6410.6	SII 1253.8	4.1129	
6440.4	SiII 1260.4	4.1098	
6460.1	SiII* 1264.7	4.1080	
6658.5	OI 1302.2, SiII 1304.4		34.9 +/- 0.2
6686.2	SiII* 1309.3	4.1067	
6735.7	NiII 1317.2	4.1136	2.3 +/- 0.2
6749.2	?		
6816.6	CII+CII* 1335		29.7 +/- 0.2
6881.7	NiII 1345.9	4.1131	7.2 +/- 0.3
7118.3	SiIV 1393.8	4.1071	14.5 +/- 0.2
7165.0	SiIV 1402.8	4.1076	8.8 +/- 0.2
7797.3	SiII 1526.7	4.1073	20.7 +/- 0.3
7831.8	SiII* 1533.4	4.1075	3.8 +/- 0.2
7908.8	CIV+CIV 1549		30.0 +/- 0.5
7963.0	?		1.1 +/- 0.2
8220.9	FeII 1608.5	4.1109	15.8 +/- 0.3
8318.8	FeII 2249.9	2.6974	0.8 +/- 0.2
8357.6	FeII 2260.8	2.6967	1.9 +/- 0.3
8536.2	AlII 1670.8	4.1090	23.2 +/- 0.3
8635.5	?		1.0 +/- 0.3
8667.7	FeII 2344.2	2.6975	6.3 +/- 0.3
8778.1	FeII 2374.5	2.6968	3.7 +/- 0.3
8811.5	FeII 2382.8	2.6980	10.5 +/- 0.3
9242.7	SiII 1808.0	4.1121	2.4 +/- 0.3

Table A.5. GRB 090529. Observed-frame equivalent widths. $z = 2.624$

Wavelength	Feature	z	EW
5532.3	SiII1526.7	2.6237	7.0 ± 1.6
5611.7	CIV1548+1550		6.2 ± 1.7

A.8. GRB 090814A

This spectrum (see Table A.7 and Fig. A.8) has only been published in a GCN circular (Jakobsson et al. 2009). It was obtained with FORS2 at VLT. Using a limited amount of absorption features we determine a redshift of 0.694 ± 0.002 .

Table A.6. GRB 090812. Observed-frame equivalent widths. $z = 2.452$

Wavelength	Feature	z	EW
4351.3	SiII 1260.42	2.4523	3.83±0.83
4365.2	SiII* 1264.74	2.4515	2.03±0.50
4499.2	OI+SiII 1303		7.59±1.02
4608.3	CII 1334.53	2.4531	6.71±0.72
4811.9	SiIV 1393.76	2.4525	1.87±0.44
4840.5	SiIV 1402.77	2.4507	1.97±0.43
5270.2	SiII 1526.71	2.4520	2.62±0.45
5292.3	SiII* 1533.43	2.4513	0.96±0.28
5348.3	CIV+CIV 1549		3.85±0.44
5414.1	?		1.48±0.46
5483.9	?		0.88±0.26
5554.4	FeII 1608.45	2.4533	6.44±0.58
5596.7	FeII* 1621.69	2.4512	1.29±0.33
5638.7	FeII*?		1.73±0.45
5722.5	CI 1656.93	2.4537	1.42±0.37
5767.6	AlII 1670.79	2.4520	3.88±0.28
6241.1	SI+Si II1808		2.92±0.42
6276.3	SiII* 1817.45	2.4534	1.10±0.37
6315.7	MgI 1827.94?		1.05±0.35
6402.2	AlIII 1854.72	2.4518	1.95±0.26
6434.3	AlIII 1862.79	2.4541	2.58±0.47
6880.7	?		4.31±0.47
9663.6	ZnII+CrII+MgI 2026		1.89±0.26
7096.8	CrII 2056.26	2.4513	0.99±0.27
7118.8	CrII+ZnII 2062		1.74±0.23
7131.4	CrII 2066.16	2.4515	0.76±0.24
7766.2	FeII 2249.88	2.4518	1.88±0.39
7805.1	FeII 2260.78	2.4524	1.84±0.32
7998.0	NiII 2316.70	2.4523	1.47±0.46
8051.7	FeII* 2333.52	2.4505	1.86±0.33
8072.8	FeII* 2338.72	2.4518	1.16±0.33
8092.6	FeII 2344.21	2.4522	3.58±0.30
8108.0	FeII* 2349.02	2.4517	0.85±0.23
8147.4	FeII* 2359.83	2.4525	1.46±0.28
8168.7	FeII* 2365.55	2.4532	1.42±0.45
8196.9	FeII 2374.46	2.4521	4.09±0.34
8224.8	FeII 2382.77	2.4518	6.24±0.36
8246.7	FeII* 2389.36	2.4514	0.85±0.28
8270.8	FeII* 2396.15	2.4517	1.70±0.34
8284.7	FeII* 2399.98	2.4520	1.55±0.49
8304.7	FeII* 2405.16	2.4529	3.80±0.46
8325.8	FeII* 2411.25	2.4529	3.14±0.42
8697.3	?		2.18±0.48
8930.5	FeII 2586.49	2.4527	4.27±0.74
8952.7	MnII 2594.36	2.4508	2.60±0.63
8975.3	FeII 2600.23	2.4517	5.57±0.48
8997.7	MnII+FeII* 2607		2.76±0.50
9018.1	FeII*+FeII* 2612		2.32±0.48
9078.6	FeII* 2629.08	2.4531	5.02±0.71
9280.6	?		1.82±0.51
9347.5	?		10.10±1.38

Table A.7. GRB 090814A. Observed-frame equivalent widths. $z = 0.694$

Wavelength	Feature	z	EW
4744.6	MgII+MgII 2800		7.08 ± 1.34
6666.1	CaII 3934.78	0.6941	4.27 ± 1.13
6720.7	CaII 3969.59	0.6930	4.58 ± 1.22

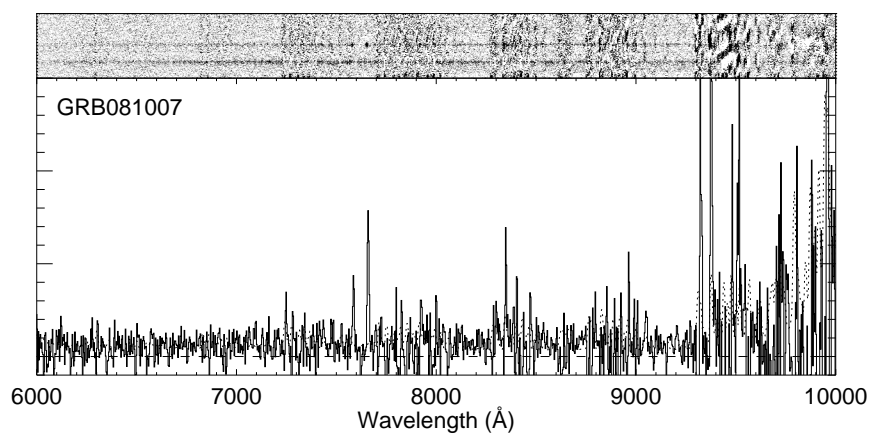


Fig. A.1. Spectrum of GRB 081007. The GRB afterglow is the central trace in the image.

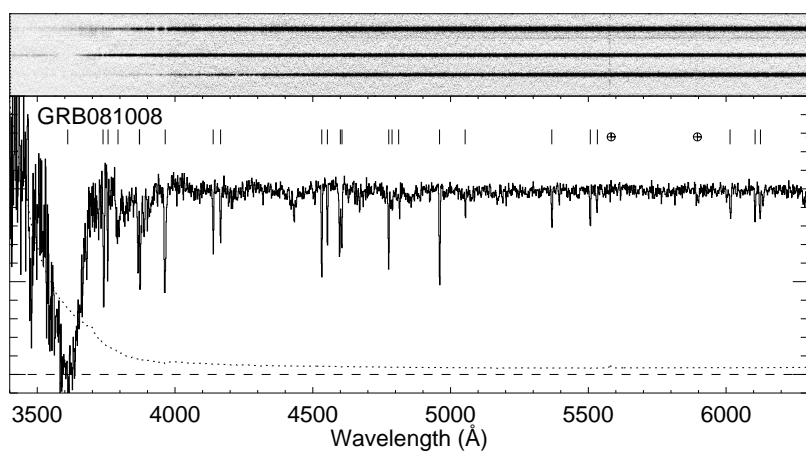


Fig. A.2. Spectrum of GRB 081008. The GRB afterglow is the central trace in the image.

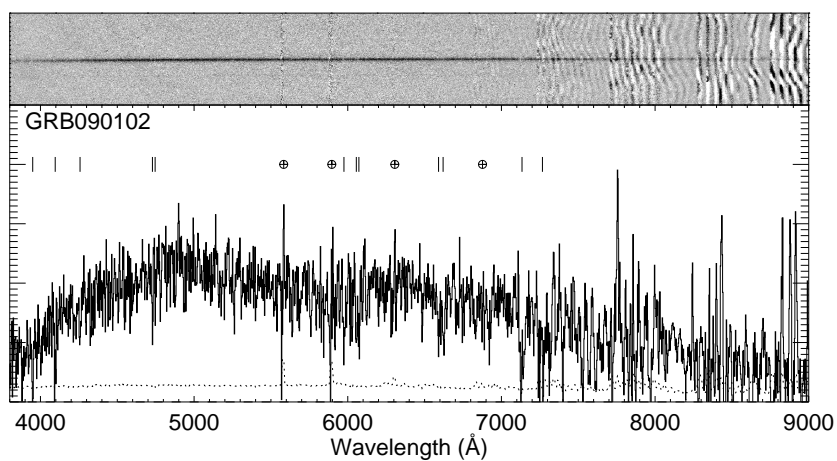


Fig. A.3. Spectrum of GRB 090102.

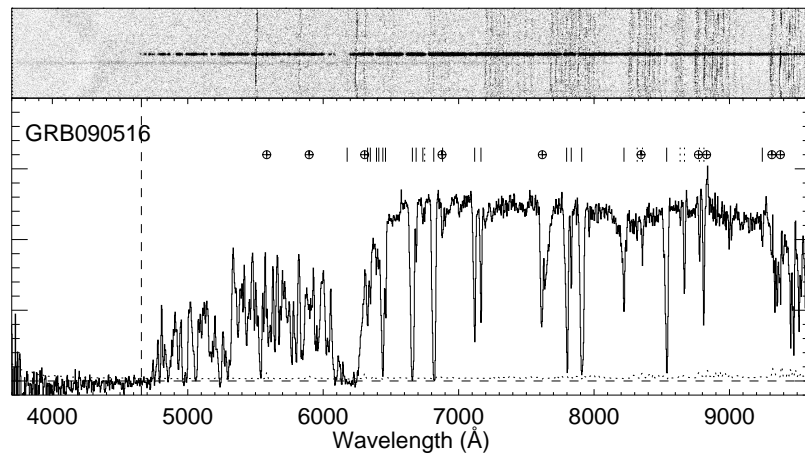


Fig. A.4. Spectrum of GRB 090516. The GRB afterglow is the bright trace in the centre of the image.

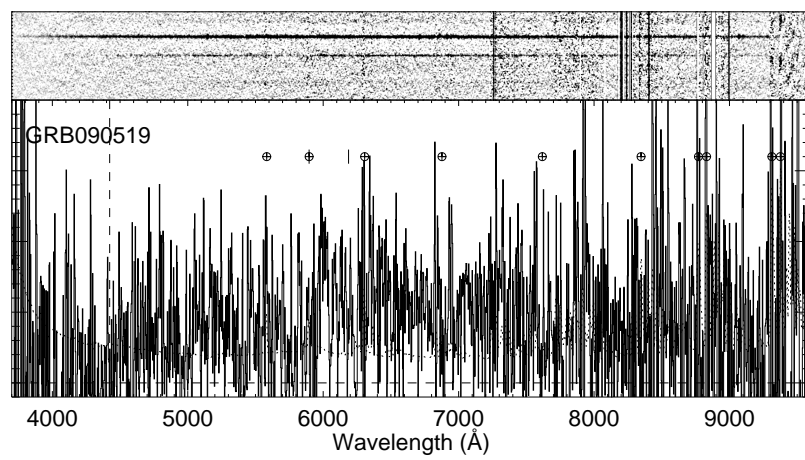


Fig. A.5. Spectrum of GRB 090519. The GRB afterglow is the weak trace in the centre of the image.

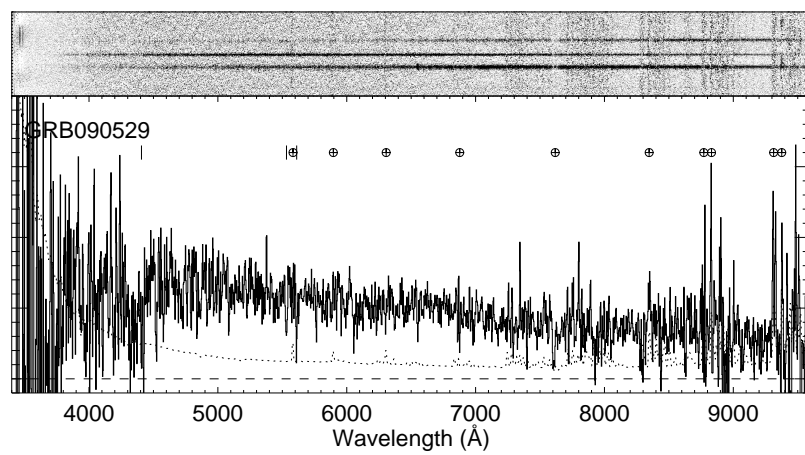


Fig. A.6. Spectrum of GRB 090529. The GRB afterglow is the central trace in the image.

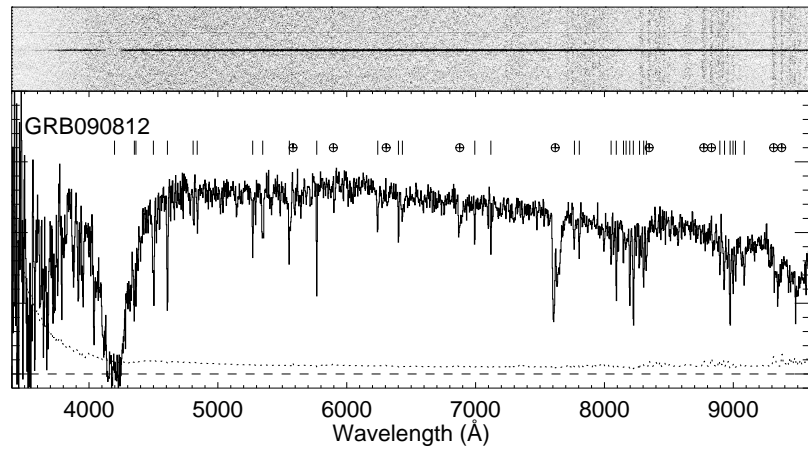


Fig. A.7. Spectrum of GRB 090812. The GRB afterglow is the central trace in the image.

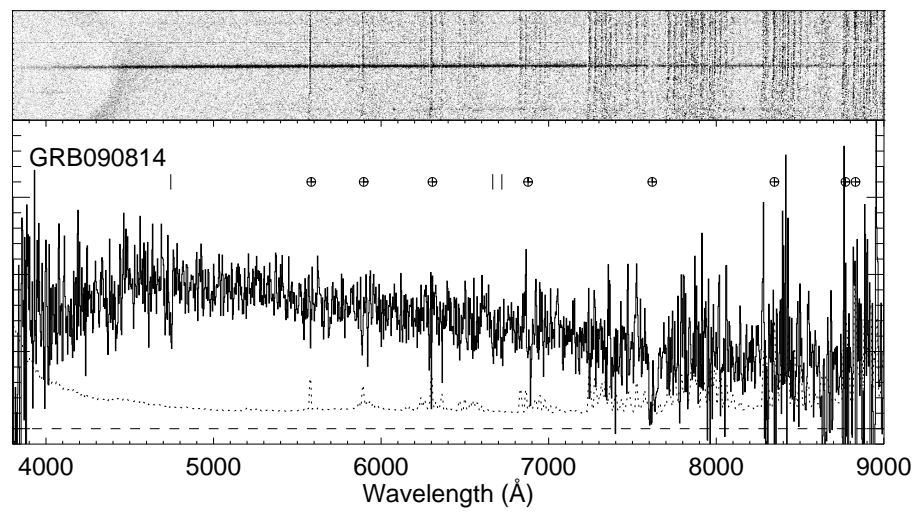


Fig. A.8. Spectrum of GRB 090814A. The GRB afterglow is the central trace in the image.

Appendix B: Line fitting

Figure B.1 shows the distribution of the EWs of each the lines. The thick black line histogram indicates only detections, whereas the dotted histogram includes also the limits. The red line is the best fit of the complete histogram with a lognormal distribution and the dashed blue line (when available) is a physical fit as described in Section 3.4. In a limited amount of features we also show in green a histogram of EWs in a sample of damped Lyman- α systems (see Section 3.3).

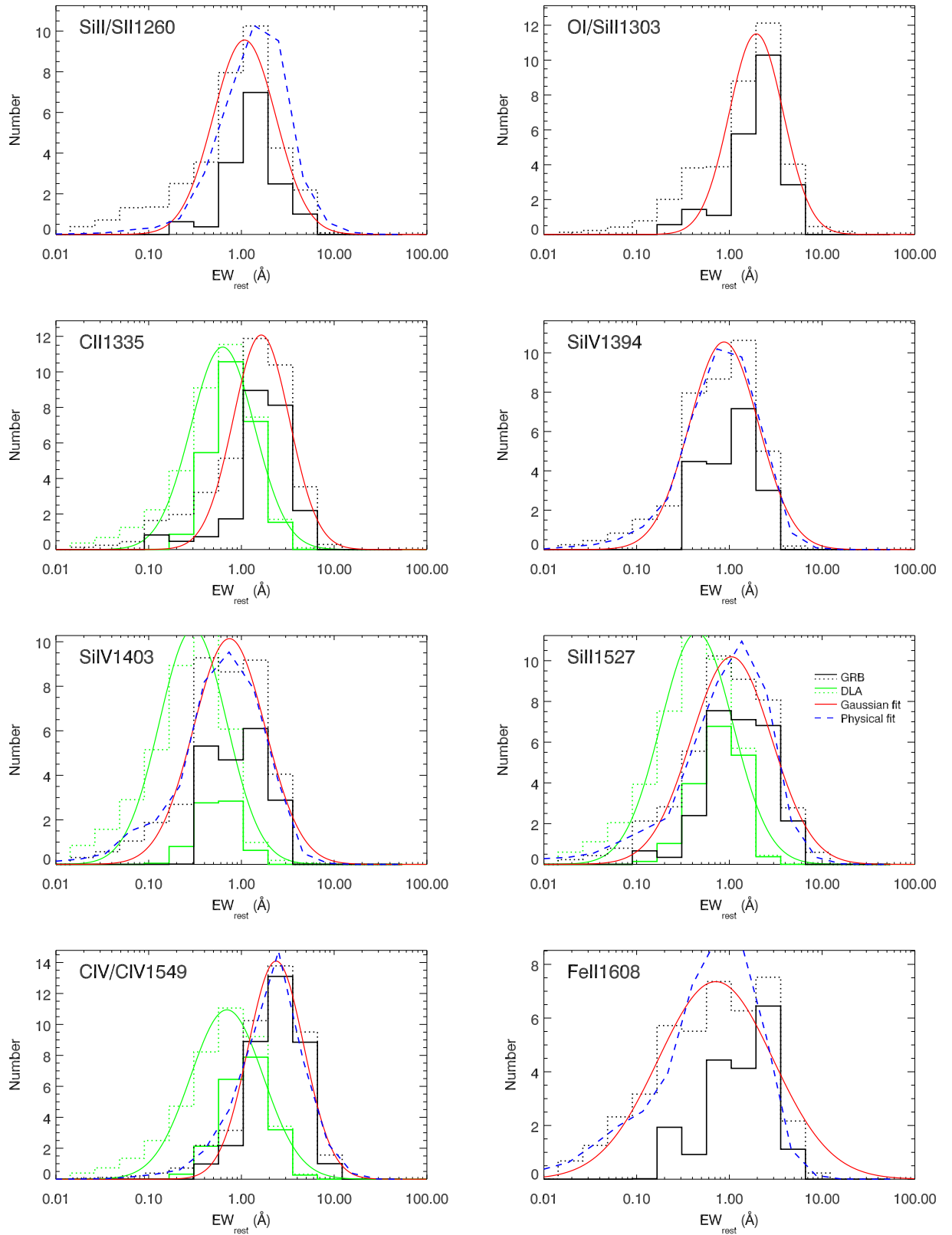
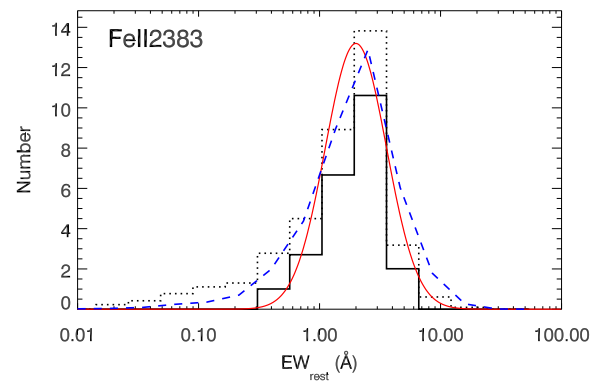
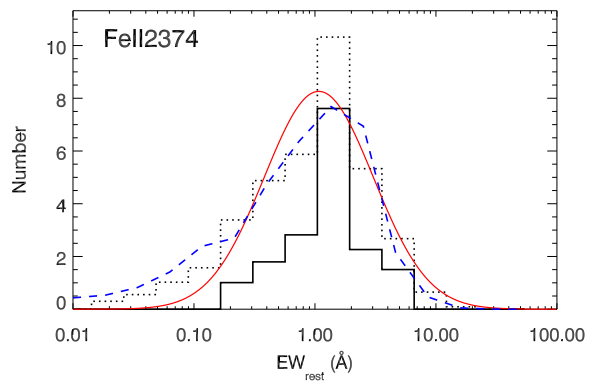
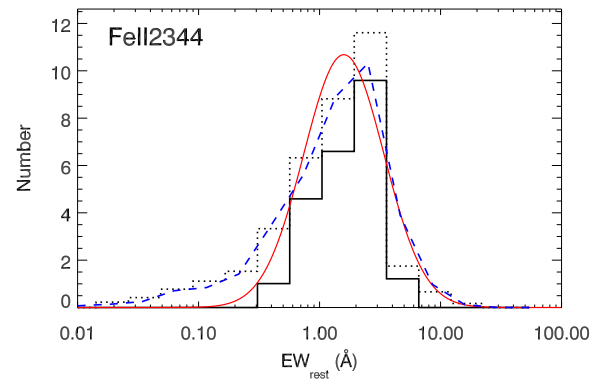
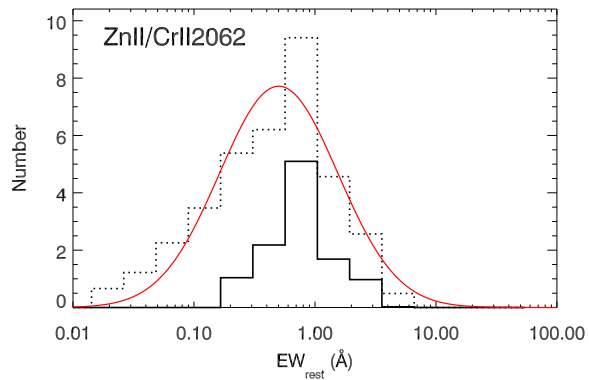
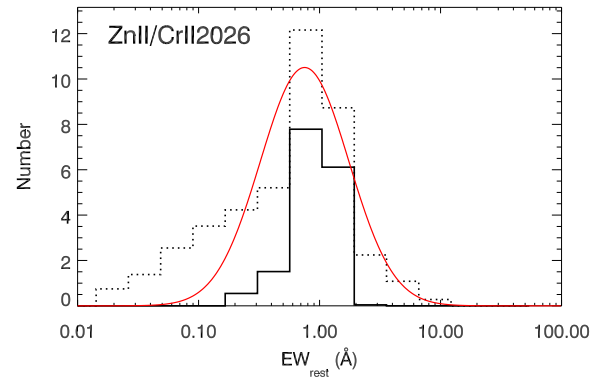
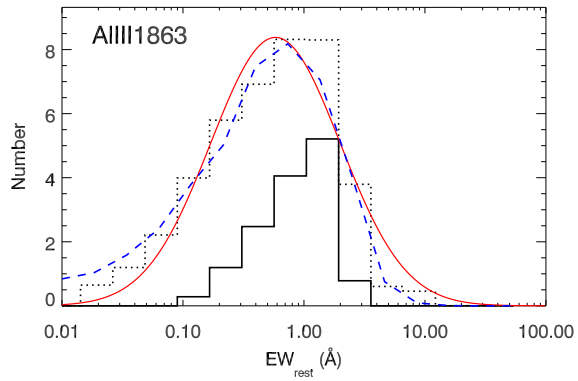
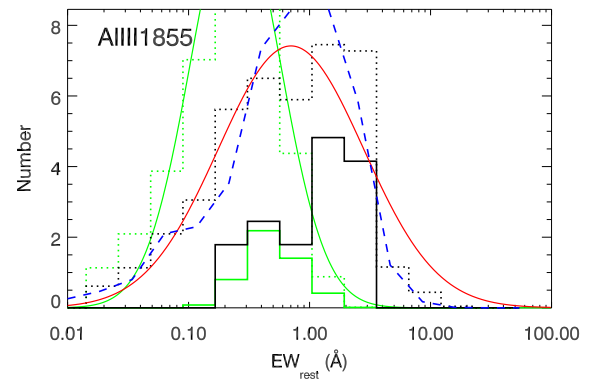
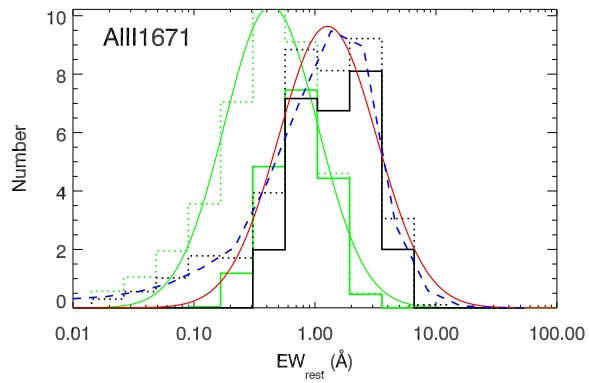
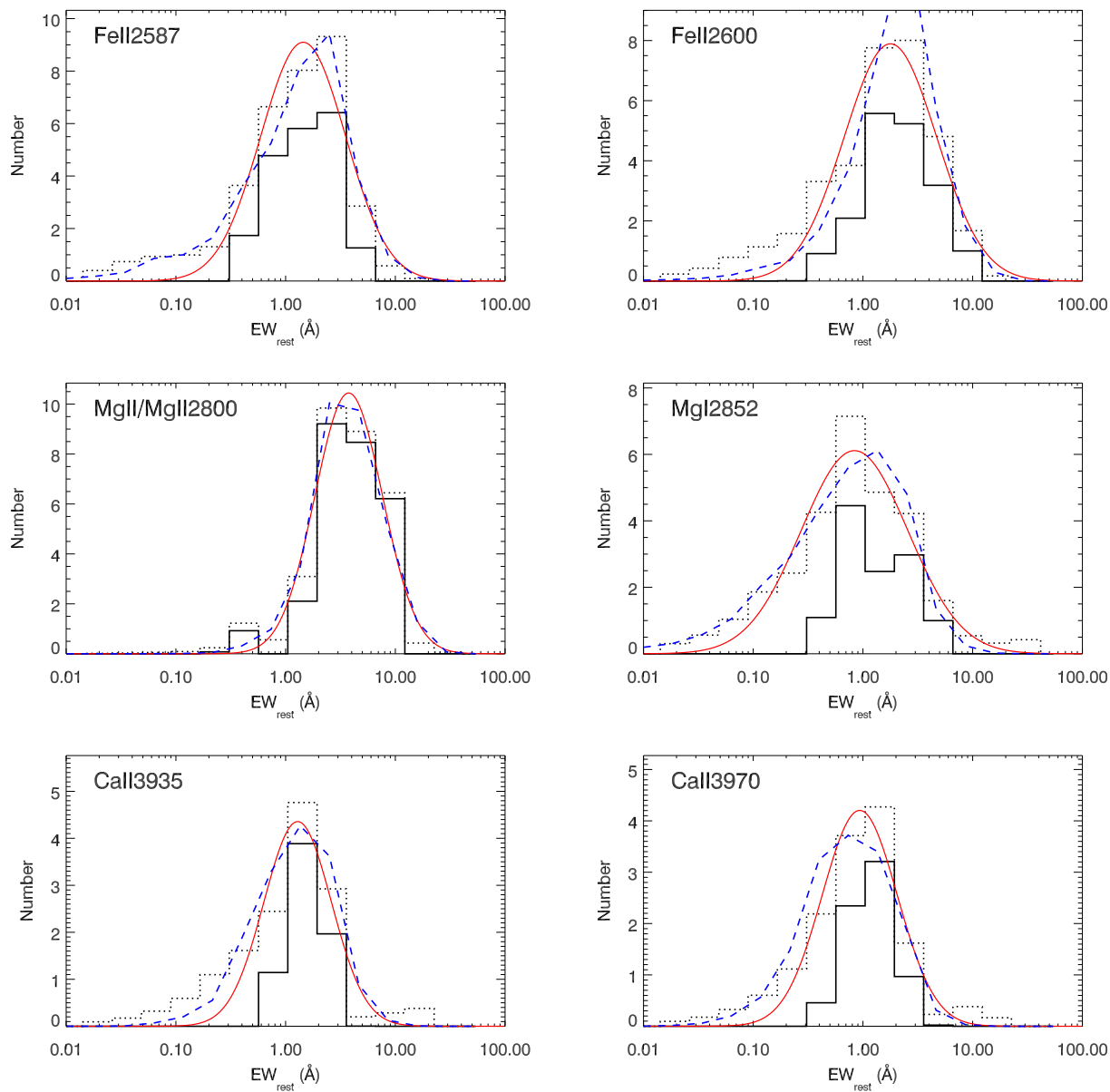


Fig. B.1. EW distribution of the different spectral features. The thick black line histogram indicates only detections, whereas the dotted histogram includes also the limits. The red line is the best fit of the complete histogram with a lognormal distribution. In some cases there is a dashed blue line for the physical fit, as described in Section 3.4. In green we show a histogram of EWs, and its correspondent lognormal fit, of a sample of DLA systems (see Section 3.3) for a subsample of lines.





Appendix C: Catalogue of EW diagrams

Figure C.1 shows a catalogue of all the GRBs, where we show the strength of each of the features and compare them with the distributions calculated in this work.

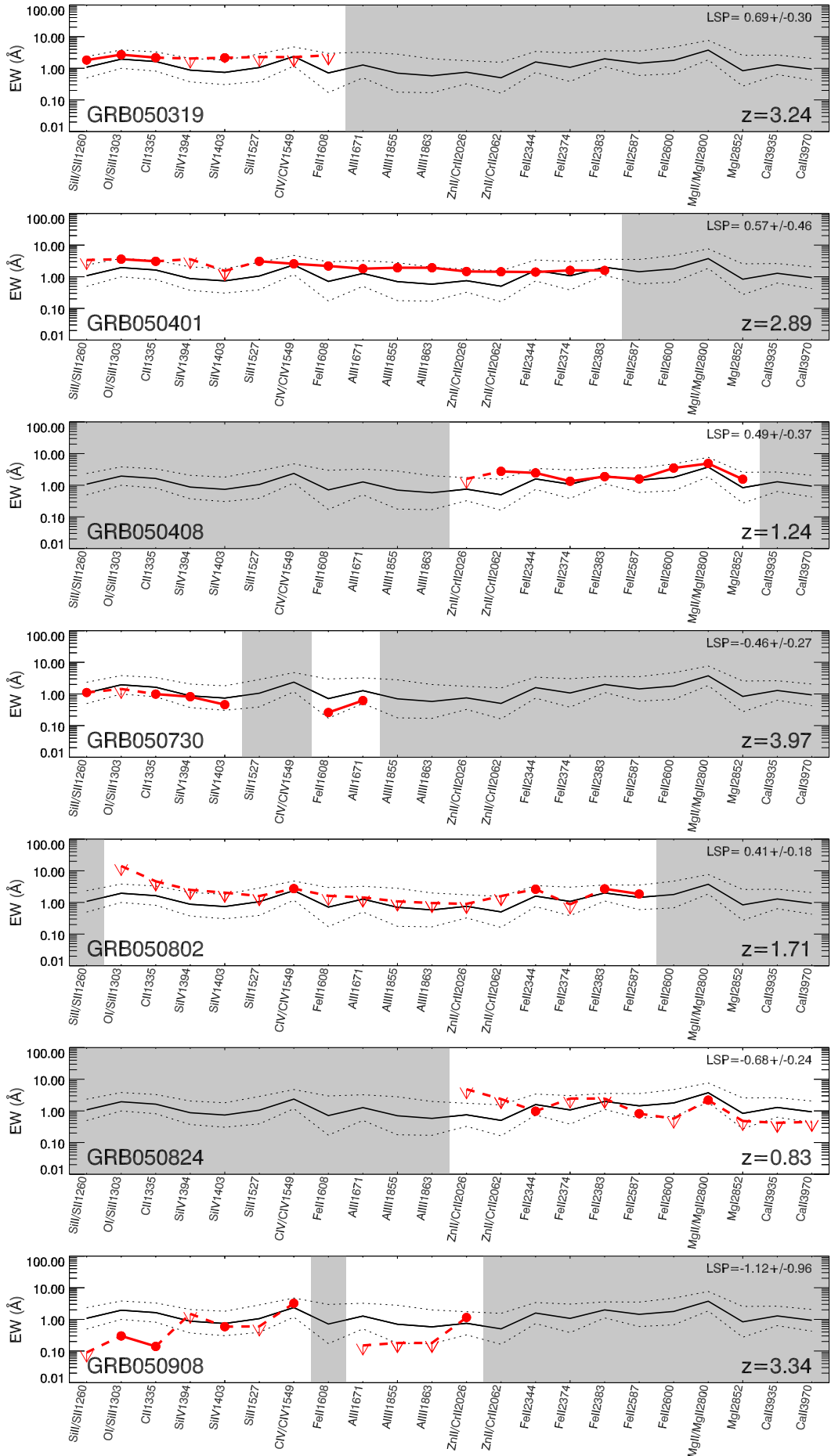


Fig. C.1. Catalogue of GRBs and their spectral features. The GRB measurements are shown in red, while the average values and standard deviations of the fits for the complete sample are drawn in red. The plots also indicate the redshift of the GRB and the LSP. The shaded regions indicate regions of the spectra where there is no data.

